UNIVERSITÀ
DEGLI STUDI
FIRENZE

DOTTORATO DI RICERCA IN
ATOMICS AND MOLECULAR PHOTONICS

Dottorato Internazionale

Ciclo XXVIII

Coordinatore Prof. Roberto Righini

A MORPHOLOGICAL BRAIN IMAGING STUDY: A NEW VERSATILE CLEARING AGENT FOR LIGHT SHEET AND TWO-PHOTON FLUORESCENCE MICROSCOPY

Settore Scientifico Disciplinare: FIS/03

Dottorando
Irene Costantini

Tutore
Prof. Francesco Saverio Pavone

Anni 2012 -2015

Contents

Part I

Introduction

Chapter 1

The neuroanatomy imaging challenge

In the last few years, a field called connectomics has garnered general interest in the scientific community. However, the concept of connectomics is not univocal. Different fields of neurobiology have their own definition of connectomics. In particular, it is possible to divide the community into two groups: those who analyze the functional activity of the brain and those who study its structural organization. For the first group, connectomics estimates and maps the functional interactions between brain regions [1]. The second group believes that connectomics consists of the reconstruction of the anatomical network of neurons [2]. Namely, on segmenting the structure of each neuron at the level of synaptic connections through the whole brain.

However, to understand the brain functionality it is necessary to know its elements and their interconnections. The structural organization of the brain affects its own mechanism, therefore, it is not possible to separate the

anatomy from the functionality.

During the realization of this analysis it is necessary to keep in mind that the structure of the nervous system is extraordinarily complicated. Individual neurons are interconnected to hundreds or even thousands of other cells forming networks that can extend over large volumes. Moreover, the brain is constituted by a great number of structurally distinct, heterogeneous, yet interconnected components.

A deeper comprehension of the brain would have an enormous impact for the whole society and will allow for the understanding of the neural basis of cognition, behavior and memory. Different international projects, such as the Human Brain Project in Europe [3] and the BRAIN initiative in the USA [4], are now studying how the brain works. Additionally, studying neuronal networks will permit a better knowledge of diseases, and thus, will open the way for new treatments.

To obtain a complete map of the neuronal network, different techniques can be used. However, since the brain architecture spans many orders of magnitude, from the cm scale of the whole brain to the nm scale of synapses, its 3D reconstruction requires the development of various approaches that analyze the structure at each level.

One of the most common technique used in neuroanatomy is electron microscopy (EM) [5]. EM obtains images at very high resolution (nm) and permits to study specific elements of the cell nanostructure obtaining information about how neurons interconnect to each other at the synaptic level. Other techniques focus their attention on a bigger scale (cm). The diffusion tensor imaging (DTI) is one of them [6]. DTI is based on the diffusion process of water in axons and can reveal tissue architecture down to the mm scale. Indeed, it allows for the mapping of neuronal fiber thought the whole brain.

Between the many techniques that address the connectomics challenge, optical methodologies are probably the most flexible. They allow for the reconstruction of large 3D volume providing micron-scale resolution imaging at relatively fast acquisition rates [7].

Most of these techniques require the sample to be fluorescently labeled [8]. Fluorescent tags have high specificity and offer the opportunity to visualize cells and tissues at high resolution. To label a sample, fluorescence proteins can be genetically encoded (transgenic animals) [9] or molecules can be carried by antibodies against specific epitopes [10], moreover, dyes can spread through the tissue with passive diffusion [11].

The first and most common approach for mapping macroscopic volume with microscopic resolution consists of slicing fluorescently-stained samples into thin sections and image them. The optical techniques used for imaging are usually confocal and multiphoton microscopy. However, both of them are not suitable for the imaging of large specimens, due to their limited imaging depth and their long acquisition time.

To optimize these processes, automated, high-throughput imaging methods, based on serial sectioning, have been recently developed. They either cut the sample by embedding it in hard resin and slicing it in ultra-thin ribbons which are imaged just after the cutting [12, 13] or by combining fixed tissue slicing with two-photon fluorescence microscopy [14]. The major limitations of these techniques are tissue deformation introduced by slicing and, intrinsically, the destruction of the sample.

An approach that does not require sample cutting is light sheet microscopy (LSM) [15, 16, 17]. In LSM the sample is optically sectioned which drastically reduce imaging acquisition time while achieving good resolution at high penetration depths. However, contrarily to the other techniques it requires the sample to be transparent. To this aim, the refractive index has

to be homogenized inside the sample through the use of a clearing agent. Methods for optical clearing can also be coupled with the other microscopy techniques, which are used to speed up acquisition, increasing the imaged volume achievable by the apparatus.

In this respect, various solutions have been used, however all of them have different characteristics and are optimized for a specific imaging technique, preventing the possibility to use them for complementary approaches. Correlative strategies are preferable, as they allow to overcome the inherent limitation of every single technique and permit to span the connectomics analysis to various scales. Indeed, a single methodology gives the answer to just one question. The coupling of various systems permits to analyze the same sample from different perspectives, obtaining a complete view of it.

The purpose of this thesis is to obtain a tool for studying the connectomics of mouse and human brains through the combination of different techniques and the investigation of various clearing approaches. After studying the advantages and the disadvantages of various procedures present in literature, the goal was achieved through the development of a new optical clearing method for multi-modal brain imaging. This protocol is based on a water-soluble, versatile, simple, rapid and inexpensive agent: 2,2'-thiodiethanol (TDE) [18, 19, 20].

The effectiveness of TDE in clearing mouse brain was characterized. Its suitability with the serial two-photon tomography [14] was demonstrated. Moreover, it was used for sample preparation in light sheet microscopy in combination with CLARITY tissue transformation [21]. Finally, TDE clearing was coupled with immunohistochemistry to stain a large volume of human dysplastic brain tissue, providing the opportunity to perform a translational analysis.

The presented strategy proposes an innovative tool for the study of con-

nectomics. TDE clearing significantly expands the application of single- and two-photon imaging on large samples and provides a novel and useful method for quantitative morphological analysis of the neuroanatomical structure of mouse and human brains.

To obtain a complete view of the state of the art, next chapters describe the anatomical organization of the central nervous system (CNS) and the major optical techniques used for imaging it. Moreover, they discuss the advantages and the disadvantages of various clearing techniques and their mechanisms to reduce light scattering in tissue.

Chapter 2

The central nervous system

The brain and the spinal cord constitute the central nervous system (CNS). The CNS is a complex organ capable of storing and processing information from a myriad of different inputs and regulating all human activity. Neuronal tissue is specialized for the conduction of electrical impulses that convey information or instructions from one region of the body to another. However, how the different parts of the brain are connected still remains unknown. This chapter analyzes the anatomical and functional characteristic of the mouse and human central nervous system.

2.1 The cells of the nervous system

The fundamental unit of the central nervous system is the neuron, which is a cell that consists of a cell body, called soma, and branches called dendrites and axon (see figure 2.1) [22, 23].

Neurons are electrically excitable cells that process and transmit information through electrical impulses, which affect their cell membrane poten-

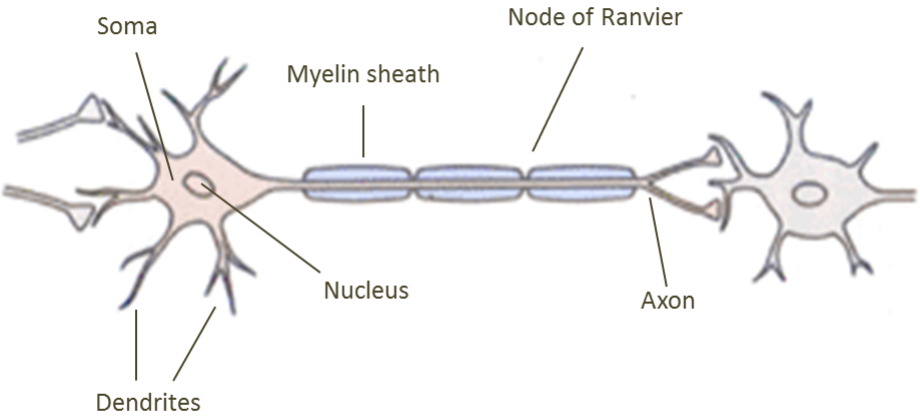

Figure 2.1: **Neuron structure** Scheme showing the general structure of a neuron. The cell body (soma) contains the nucleus and gives rise to two types of branches: axon and dendrites. The axon is a process covered by a fatty sheath of myelin that is interrupted at regular intervals by the nodes of Ranvier, and transmits the electric signal. The axon of one neuron transmits signals to another neuron at a site called synapse. The dendrites collect information and transmit it to the cell body where it is integrated with signals from other neurons. The image is taken from [22].

tials and lead to chemical signals. Normally the cell membrane potential is $-70mV$, and the cell is said to be polarized. When an electrical impulse affects the membrane potential of a neuron's dendrite, the potential rapidly increases causing the depolarization of the cell. If the depolarization reaches a defined threshold value it elicits an action potential. Special types of voltage-gated ion channels embedded in the cell's membrane are responsible for this mechanism. When the neuron is polarized these channels are shut, but they open if the membrane potential increases. In this way, they allow for an inward flow of sodium ions, which changes the electrochemical gradient of the cell raising the membrane potential. During an action potential, the membrane potential reaches the threshold value. As a consequence, more channels open producing a greater electric current that travels along the entire length of the axon and transmits the signal to other neurons [24]. This signal is self-sustained, once it is generated it will travel across the entire length of the neuron and will transmit the information to another cell. A single neuron can connect the different areas of the brain even located very far away from each other. Indeed, to increase the speed by which action potentials are conducted, axons are wrapped in a fatty, insulating sheath of myelin produced by Schwann cells (a specific type of glia cells). The sheath is interrupted at regular intervals by the nodes of Ranvier in correspondence to the end of a Schwann cell and the beginning of the next one [25].

The specialized connections where the information between neurons are exchanged are called synapses. A synapse is a region where the axon from the neuron transmitting the signal connects to a dendrite of the target cell. On axons it is possible to recognize a structure called varicosity while on dendrites there are protrusions called spine. There are two types of synapses: electrical synapses and chemical synapses. The first type transmits directly

the electrical impulse to other cells through channels called gap junction. The second uses chemical mediators called neurotransmitters that activate ion channels on the membrane of a target neuron [26]. The nerve cell transmitting the signal is called presynaptic cell while the cell receiving the signal is called postsynaptic cell.

Apart from neurons, the nervous system is composed of another class of cells: the glial cells (glia). Glial cells have different roles in the nervous system. Astrocytes support neurons by providing the brain structure; contribute to make impermeable brain capillaries; guide migrating neurons and direct the outgrowth of axons during the brain's development. Oligodendrocytes and Schwann cells remove debris and produce myelin. Microglia cells promote efficient signaling between neurons, for example, by taking up transmitters released in the synaptic space [27].

In the brain it is possible to identify two kinds of tissues, the gray matter and the white matter. The gray matter contains the cell bodies of neurons and most of it is concentrated on the surface, or cortex, of the brain. It has a gray/brown color which comes from the capillary blood vessels and the neuronal cell bodies. The connecting structures between various gray matter areas of the brain form the white matter. It is composed of axonal nerve fibers covered by myelin sheaths that give it its distinctive color. The inner part of the brain is mostly white matter, but inside it there are also some gray matter areas constituted by small groups of neurons, that work as junctions along signaling pathways [23].

2.2 Central nervous system anatomy

At a larger scale, the central nervous system is divided into seven main parts [22, 23]. They are present in both human and mouse species (fig-

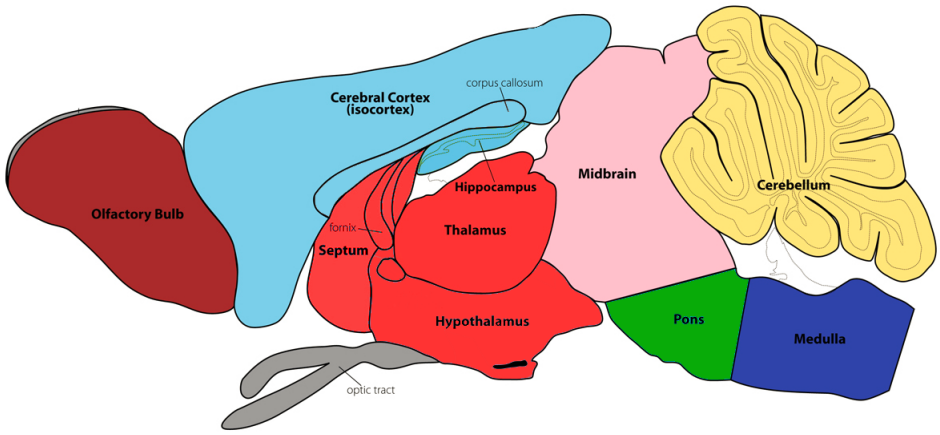

Figure 2.2: **Mouse central nervous system anatomy** The main structures of the mouse central nervous system are: the spinal cord, the medulla oblongata (dark blue), the pons (green), the cerebellum (yellow), the midbrain (pink), the diencephalon(red), and the cerebral hemispheres (light blue). In addition, a large part of the rostral brain is constituted of the olfactory bulbs (brown).

ure 2.2 and 2.3). The spinal cord serves as a conduit for signals between the brain and the rest of the body. It also controls simple musculoskeletal reflexes without input from the brain. The medulla oblongata lies above the upper end of the spinal cord. Besides being a conduit for fibers running between the spinal cord and other regions of the brain, it contains control centers for involuntary functions such as blood pressure, breathing, and digestion. Just above the medulla there are the pons and the cerebellum. The pons relays information between different regions of the brain and the cerebellum, which processes sensory information and motor skills. The next segment, the midbrain, is primarily responsible for eye movement and auditory reflexes. Next the midbrain lies the diencephalon, which is

composed of two major parts: the thalamus, that processes and integrates all information going to the cerebral cortex; and the hypothalamus, that is critical for body homeostasis, visceral function, and endocrine function. The highest regions of the brain are the cerebral hemispheres, which include the basal ganglia (motor performances), the hippocampus (memory storage), the amygdaloid nuclei (emotional states), and the cerebral cortex. Moreover, in the mouse brain, a large part of the rostral part of the brain is dedicated to the olfactory bulbs that are involved in the sense of smell (olfaction) [22].

The cerebral cortex is the most important structure of the gray matter, it constitutes the outermost layer of the brain and is responsible for conscious sensation and voluntary movements, as well as advanced functions such as thinking, learning and controlling emotion. It is composed of two hemispheres that are separated by a prominent central fissure. In humans each hemisphere is made of four lobes (see figure 2.3). The frontal lobe, located in the front part, plays an important role in reasoning, planning, language, memory and motor control. The parietal lobe, behind the frontal lobe, integrates sensory information and processes visuo-spatial stimuli. The temporal lobe, on the most lateral parts of the cortex, is involved in auditory processing as well as language and vision related functions. The occipital lobe occupies the rear part of the cortex and is the processing center of visual stimuli [22] [23].

Since the cerebral cortex has such an important role, the next section will focus on its microscopic structural anatomy.

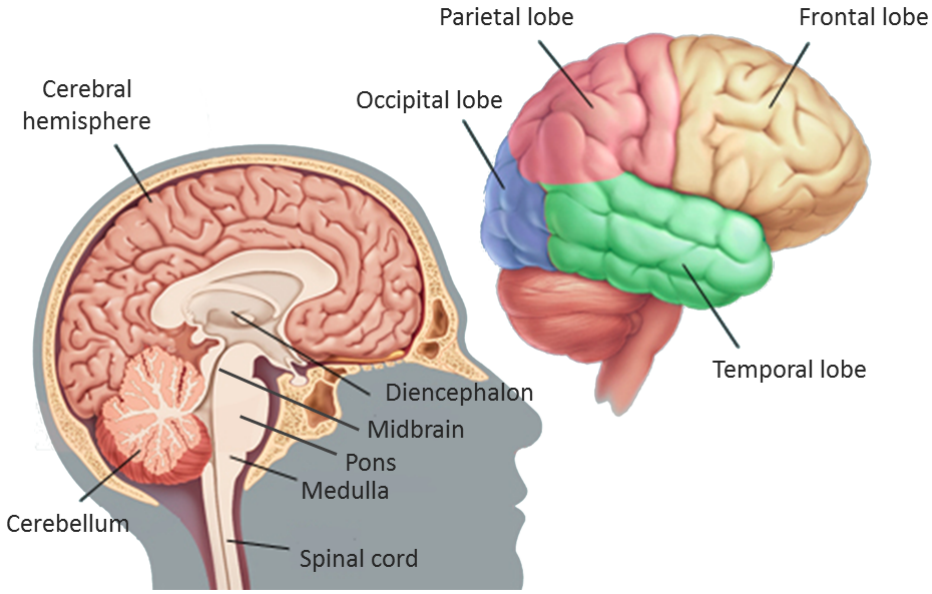

Figure 2.3: **Central nervous system anatomy** On the left scheme, the main structures of the central nervous system are represented: the spinal cord, the medulla oblongata, the pons, the cerebellum, the midbrain, the diencephalon, and the cerebral hemispheres. The right schematic drawing shows the position of the four lobes of the cerebral cortex [28].

2.3 The cerebral cortex

The cerebral cortex is organized into six horizontal layers [29, 22], numbered from the outer surface of the cortex to the white matter (figure 2.4).

Cortical layers contain two distinct neuronal types: pyramidal and non-pyramidal neurons [30]. Pyramidal cells are the projection neurons of the cerebral cortex (i.e., neurons whose axons extend from one region to distant regions of the CNS). They have a triangular soma and a characteristic dendritic arborization pattern. These cells use glutamate as excitatory neurotransmitter. Non-pyramidal cells are the cortical interneurons, a heterogeneous group of cells that display a broad range of morphologies and molecular identities. These neurons transmit signals using the neurotransmitter γ-Aminobutyric acid (GABA) and also one or more neuropeptides such as somatostatin, neuropeptide Y and cholecystokinin [31].

Individual layers have different roles and vary in relative thickness among cortical regions. Though each cortical region has a different laminar organization, the most common is the following.

The first layer is called molecular layer. In this layer there are no cell bodies, but it is occupied by dendrites of cells located deeper in the cortex, and axons that travel through the layer or form connections in this layer. The layer II is composed of interneurons. They are small spherical cells called granule cells. This layer is called external granule cell layer. Layer III, otherwise, is called external pyramidal cell layer, because it contains pyramidal cells. Layer IV, like layer II, is made up primarily of granule cells and is called internal granule cell layer. Layer V, the internal pyramidal cell layer, contains mainly large pyramidal cells, projections and long association outputs. Finally, layer VI is a layer constituted by heterogeneous types of neurons and is thus called the polymorphic or multiform layer. It blends

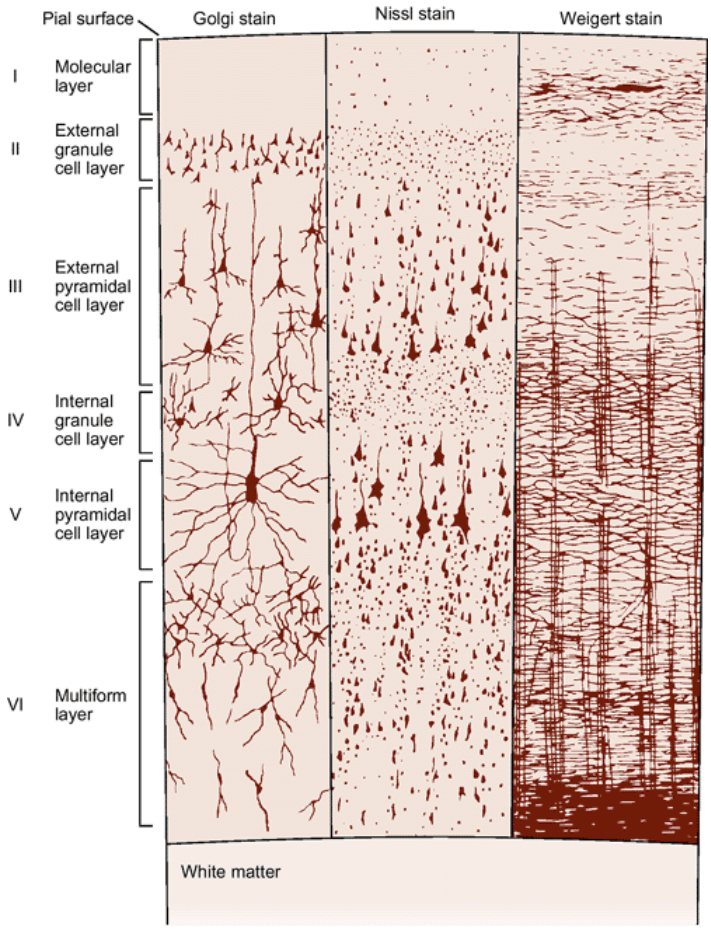

Figure 2.4: **Layers of the cerebral cortex** The cerebral cortex is organized into six cell layers. In the image, different stainings are represented, they underline the different tissue characteristics of each layer. The Golgi stain reveals neuronal cell bodies and dendritic trees. The Nissl method shows cell bodies and proximal dendrites. A Weigert stain for myelinated fibers reveals the pattern of axonal distribution. The image is taken from [29].

into the white matter that forms the deep limit of the cortex and carries axons to and from the cortex [29].

Layers assume their organization during development. Stem cell precursors give rise to all neurons through differentiation and migration from their birthplaces in the embryo to their final positions. Once the position is reached, immature neurons organize axons and dendrites to generate synapses [22]. The development of the cerebral cortex is a complexly organized process. Disruption of any of the steps that contribute to this process (neuronal proliferation, migration or layer organization), can result in a wide range of developmental disorders.

As shown in this chapter the structure of nervous tissue is very complicated. Different methods should be used to study the anatomical organization of all the different networks that constitute the brain. In the next chapter there will be a description of some of the optical techniques that can be used for brain imaging.

Chapter 3

Optical imaging techniques in neuroscience

One of the main methods to produce images of the brain is optical microscopy. This field has started at the end of the 16th century with Zacharias Jansen's first microscope, and since then, many developments have been done to increase microscopes performances and explore different contrast mechanisms.

To make an object distinguishable from other objects within the same field of view, it is necessary that there is a difference regarding color or brightness, and that there is the contrast.

The main contrast mechanisms are based on transmittance (bright field microscopy), phase shift (phase contrast microscopy) and scattering (dark field microscopy). It is however fluorescence that, thanks to its high specificity and sensitivity, became the most popular source of contrast in biological microscopy (Figure 3.1).

This chapter describes the physical principles of fluorescence microscopy

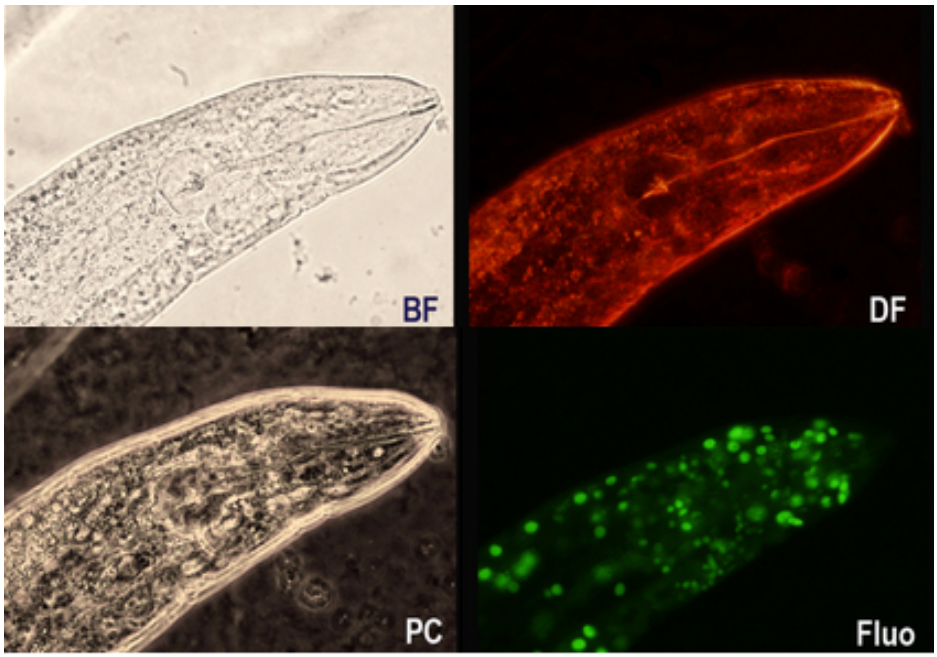

Figure 3.1: **Types of light microscopy** To improve specimen contrast different techniques can be used. In bright field (BF) microscopy, the sample is illuminated via transmitted white light. The dark field (DF) microscope collects only the light scattered by the sample (the image is taken with a red filter). Instead in phase contrast (PC) microscopy, the phase shift reveals index mismatch in the sample and creates changing in brightness due to variation in refractive index in transparent samples. Fluorescence microscopy (Fluo) highlights only the labeled structures of the tissue ensuring high specificity and sensitivity [8].

and focuses on the most common techniques used for high-volume 3D reconstruction.

3.1 Fluorescence

Fluorescence is the spontaneous emission of light by any molecule that has previously absorbed light. To illustrate this process, an Alexander Jablonski diagram is routinely used (see figure 3.2) [32, 33]. A typical Jablonski diagram graphically displays the energy states of a molecule. Electrons can lie in different electronic states of increasing energy, for example the ground state ($S0$), the first excited state ($S1$), and higher excited states (Sn). Each of these electronic energy levels is divided into vibrational energy level depicted by 0, 1, 2, etc. that are split into different rotational levels. The transitions, that is the absorption and emission of photons between states are illustrated as vertical lines in this graph. For each given fluorophore there is a range of wavelengths, the *excitation spectrum*, that can excite it.

The energy of the absorbed photon is inversely related to the exciting wavelength:

$$E = \frac{hc}{\lambda} \tag{3.1}$$

In this equation h is Plank's constant and c and λ are the speed and the wavelength of light in vacuum, respectively. By absorbing the energy of the incident photon an electron of the fluorescent molecule is raised from its ground state into an higher electronic energy level. Before the electron decays back to $S0$, a fraction of the absorbed energy gets dissipated due to internal conversion and vibrational relaxation. For that reason, the emitted photon has a lower energy compared to the one that has excited the

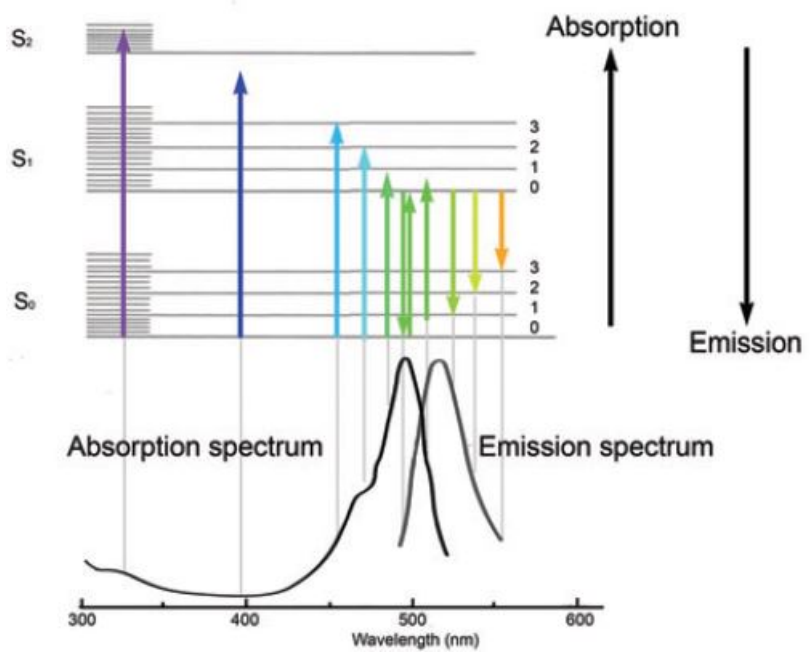

Figure 3.2: **Jablonski's diagram** Scheme depicting the spectral characteristics related to absorption and emission of energy by a molecule. Molecules, not absorbing energy are mainly confined to the lowest vibrational states of the ground state $S0$. Each gray vertical line aligns the spectrum with the energy of the absorbed (arrows pointing up) or emitted (arrows pointing down) photons. The arrows are colored to represent the wavelength of the photons. From Lichtman et al [32].

molecule. This is called the *Stokes shift* and varies from one fluorophore to another. The difference created with the *Stokes shift* between the exciting and emitted wavelengths, is the property that permits the easy discrimination of the generated fluorescence from the excitation light through a dichroic filter. Therefore, it is possible to see only the objects that are fluorescent while all the rest provides a black background.

Despite many organic substances have intrinsic fluorescence (autofluorescence), fluorescence microscopy usually exploits synthesized compounds (fluorophores) or fluorescent proteins such as GFP (green fluorescence protein). To obtain a good image it is necessary that a molecule has a high quantum yield:

$$q = \frac{k_r}{k_r + k_{nr}} \quad k_r = \frac{1}{\tau_r} \quad k_{nr} = \frac{1}{\tau_{nr}} \tag{3.2}$$

Where k_r is the rate of photons that decay with a radiative process and k_{nr} is the rate related to non-radiative processes. They are inversely proportional to the electron life-time (τ_r and τ_{nr} respectively). Electrons of endogenous substances usually fall back to $S0$ without emitting fluorescence (non-radiative decay). On the other side, fluorophores have a high quantum yield and permit a radiative decay. However, the fluorescence intensity of a molecule is not constant. Different mechanisms such as excited state reactions, energy transfer, complex-formation, and molecular collision can decrease the quantity of emitted photons producing an effect called quenching.

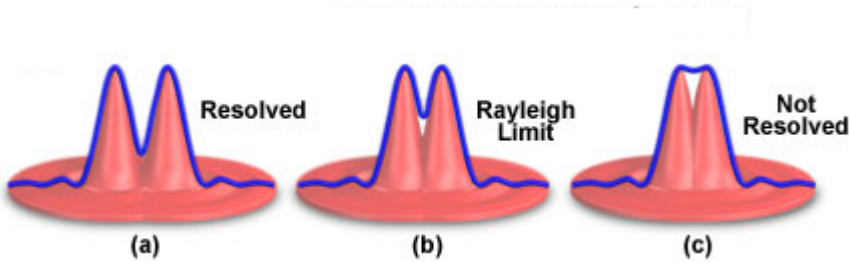

Figure 3.3: **PSF and resolution** Point spread functions of two adjacent points. (a) Resolved points (b) Rayleigh limit between two points (c) Unresolved points. Image taken from [34].

3.2 Optical resolution

The ability of an imaging system to resolve small details in the object is quantified by resolution. This is defined as the shortest distance between two points that can still be distinguished as separate entities [8]. All optical microscopes are limited by diffraction in the resolution they can achieve. Diffraction is a phenomenon that occur when light encounters an obstacle. Because in every optical imaging system light propagation is limited by finite apertures, point light sources appear as diffraction patterns. The three-dimensional representation of this diffraction pattern is known as point spread function (PSF).

To quantitatively define resolution there are several criteria. The most common criteria considers two points as resolved when the maximum of the PSF of one coincides with the first minimum of the other. This distance (r_{min}) is called Rayleigh limit (see figure 3.3) and is given by:

$$r_{min} \approx \frac{0.6\lambda_0}{NA} \tag{3.3}$$

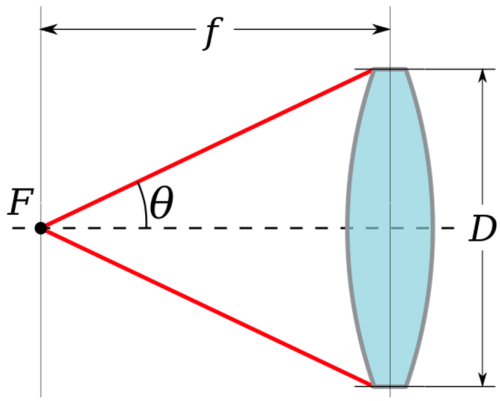

Figure 3.4: **Numerical aperture** The NA of an optical system is a number that characterizes the angle over which the system can accept or emit light in dependence of the refractive index of the medium. θ is the half-angle of the maximum cone of light that can enter or exit the lens. f is the focal length of the lens. D is the diameter of the entrance pupil. F is the focal point. Image taken from Hecht [35].

Where the numerical aperture (NA) of a lens is defined as:

$$NA = n \times sin\theta \tag{3.4}$$

Where n is the refractive index of the medium in which the lens is working, and θ is the half-angle of the maximum cone of light that can enter or exit the lens (figure 3.4) [35].

It is also possible to define an axial resolution (z_{min}), that is given by the equation:

$$z_{min} \approx \frac{n\lambda_0}{(NA)^2} \tag{3.5}$$

However, since light detectors (such as cameras, photomultiplier tubes, etc.) are planar, they integrate light coming from all different axial positions in the sample. Most of the planes (basically all outside the z_{min} range defined above) are out of focus, their contribute only as image blur. Systems that are capable of discriminate light coming from different z positions are said to perform optical sectioning, as opposite to the physical sectioning used in standard wide-field microscopy. Microscopes performing optical sectioning are considered in next sections.

3.3 Confocal and two-photon microscopy

The most common fluorescence technique is the wide-field microscopy. In this kind of microscopy, a large area of the sample is illuminated with collimated light and the fluorescence is detected by a camera. In this way, planes located above and below the plane conjugated with the detector are also illuminated and out-of-focus fluorescent molecules give rise to image blur that lowers the contrast. To avoid this effect, fluorophores excitation should be restricted to the plane conjugated with the detector, or the system should be able to distinguish in-focus and out-of-focus light. To this end, various approaches have been developed. Here, the confocal microscopy and the two-photon microscopy approaches will be discussed (figure 3.5).

3.3.1 Confocal microscopy

In confocal microscopy (CM), wide-field illumination is replaced by a focused beam [37]. The light is focused by the objective into a single spot located in the focal plane into the specimen. The fluorescence generated in the sample at the focal position is collected by a fast detector, usually

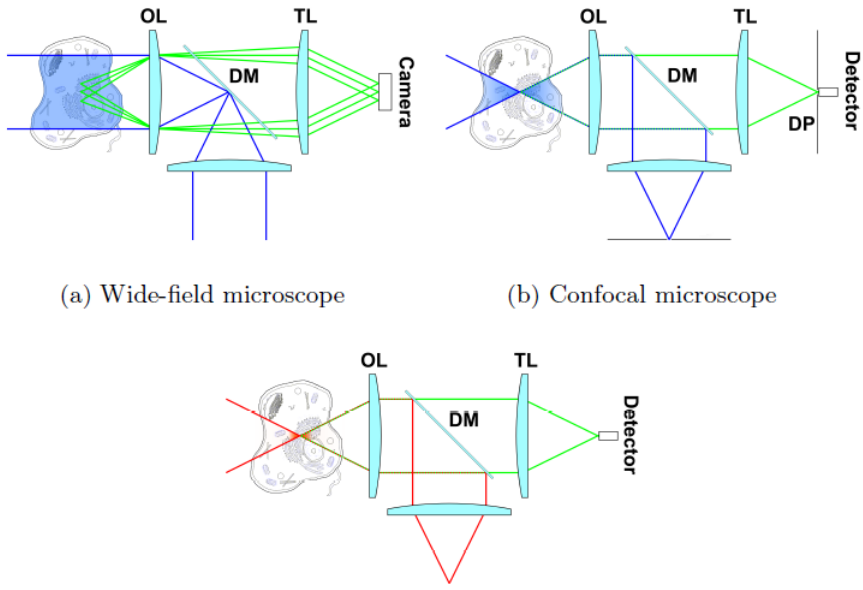

(a) Wide-field microscope

(b) Confocal microscope

(c) Two-photon microscope

Figure 3.5: **Fluorescence microscopy techniques** Simplified scheme of different kinds of fluorescence microscopes. In (a) there is the wide-field fluorescence scheme. To obtain the information from the focal plane the whole sample is illuminated. With the confocal approach (b) only the fluorescence from the focal spot reaches the detector. The two-photon microscope (c) confines the excitation to focal plane avoiding illumination of out-of-focus areas. OL = objective lens, TL = tube lens, DM = dichroic mirror, DP = detection pinhole. Single-photon excitation light is in blue, two-photon in red while fluorescence emission is in green. From [36].

a photomultiplier tube (PMT). To obtain the 2D image the laser beam is consecutively shifted by scan mirrors to a large number of raster positions. The most important characteristic of this microscope is the presence of a spatial pinhole placed in front of the detector. It prevents light originating from above or below and lateral the focal plane of the sample from reaching the PMT (see figure 3.5). The elimination of out-of-focus signal leads to the optical sectioning of the sample and enables acquisition of unblurred images. A drawback of confocal microscopy is the strong excitation light required, that can cause fluorescence quenching. Moreover, the CM needs an objective with a high NA for the collection of photons, and that limits the working distance, and, therefore, the depth achievable with this technique.

3.3.2 Two-photon fluorescence microscopy

Two-photon fluorescence microscopy (TPFM) is based on the principle that the excitation of a fluorophore can be achieved by the nearly simultaneous absorption of two photons of about half of the energy required for single-photon excitation. The probability of two-photon absorption is quadratically dependent on the intensity of the incident light. To generate sufficient signal, excitation light intensity has to be concentrated in space and time and this occurs only in the focal plane. Away from the focus, the probability drops off rapidly so that elsewhere in the sample the excitation is very unlikely (see figure 3.5 and 3.6, [38, 39]). Indeed, only ballistic photons lead to fluorescence, there is no background and, therefore, the excitation light can penetrate deep into the specimen to the plane of focus.

The lack of out-of-focus excitation in non-linear microscopy carries to a spatial resolution that is nearly identical to the one of confocal microscopy without the use of a pinhole. The long wavelengths (infrared region, IR)

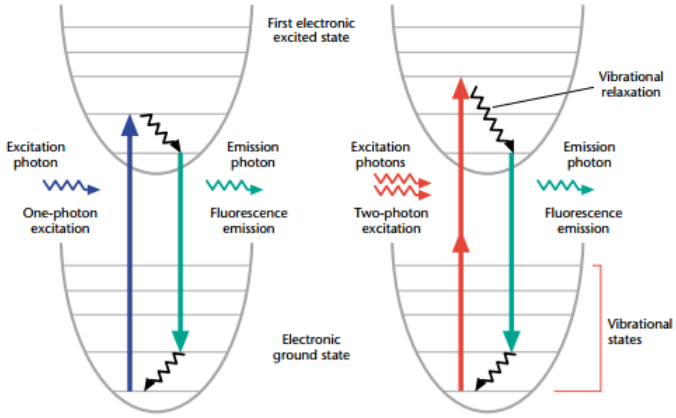

(a) Jablonski diagrams

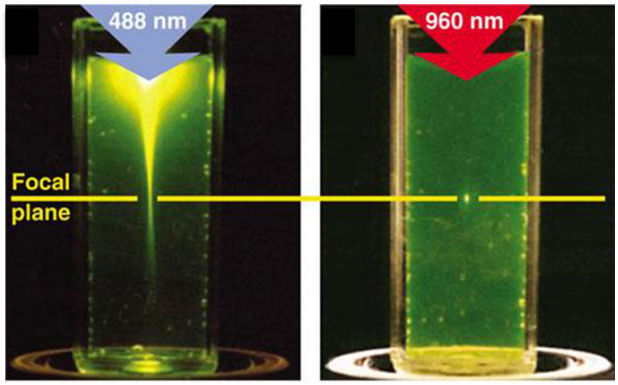

(b) Excitation volume

Figure 3.6: **Localization of fluorescence by two-photon excitation** (a) Jablonski diagram of one-photon (left) and two-photon (right) excitation. One-photon excitation occurs through the absorption of a single photon. Two-photon excitation occurs through the absorption of two lower-energy photons via a virtual state. From [39]. (b) On the left, single-photon excitation of fluorescein by focused 488 nm light. On the right, two-photon excitation using focused femtosecond pulses of 960 nm light. From [38].

used in TPFM are generally less phototoxic to living tissue and lead to a less quenching. Moreover, in the IR region biological tissues are more transparent allowing to reach higher imaging depth compared to CM. Consequently, the maximum depth achievable in living animals is $\sim$800μm [39]. However, it drastically decreases in fixed samples (300μm) [40]. That limits the imaging analysis of high volume samples such as the whole mouse brain.

3.4 Serial sectioning methods

The growing need of obtaining whole-brain reconstruction has led to the development of new approaches that combine different techniques. One method consists in obtaining automatic microscopes for large datasets analysis based on the integration of imaging and tissue sectioning.

It is possible to distinguish two similar processes based on the microscope used. One of them is micro-optical sectioning tomography (MOST and fMOST for fluorescence microscopy) [12, 13] that uses a single-photon microscope coupled with tissue serial sectioning. Another is the serial two-photon (STP) tomography [14], it combines two-photon fluorescence microscopy with the serial sectioning of the sample.

These methods are characterized by the presence of automated high-throughput instrumentation. In particular, a motorized platform is present under microscope objective for moving the sample allowing top-view mosaic imaging. Before every cycle of acquisition, a sectioning step is performed followed by a mechanical removal of the imaged tissue.

Samples preparation is different between the two techniques. In fMOST the brain is embedded in a hard resin that allows to cut the sample in ultra-thin sections (1 μm) with a diamond knife (figure 3.7). In this technique, the preparation of the sample requires time and effort but permits very precise

cuts. The absence of distortions avoids alignment problems and guarantees a complete reconstruction of the whole brain.

Instead, in STP, the brain is fixated with paraformaldehyde. This allows for embedding the tissue in agar and performing the sectioning with a vibratome (figure 3.7). This approach doesn't require specific efforts in preparing the sample, however, it presents a disadvantage. Due to tissue deformations introduced by slicing, imaging can't be done near the tissue cuts. It is preferable to image 50 μm below every cut. Moreover, since the tissue is fixed, the imaging penetration depth achievable with the two-photon fluorescence microscope is few hundreds of μm. To obtain the complete reconstruction of large volumes in a relatively short time (hours to days in dependence of the resolution) Ragan et al. [14] found a compromise between slicing and imaging. Whole brain tomography was obtained cutting every 100 μm and imaging 50 μm below the tissue surface, leading to the 95% loss of information.

Although these approaches allow big sample reconstruction with very high resolution (figure 3.8), they require long acquisition times (days up to weeks). Furthermore, these techniques intrinsically destroy the sample during imaging.

To overcome these downsides another approach, that does not require sample cutting, can be used: the light sheet microscopy (LSM).

3.5 Light-sheet microscopy

Light-sheet microscopy (LSM) is a fluorescence microscopy technique that uses a thin sheet of light to illuminate the specimen, performing optical sectioning instead of physical sectioning [15, 16, 42, 43]. In detail, during LSM the sample is illuminated with a thin sheet of light confined in the focal

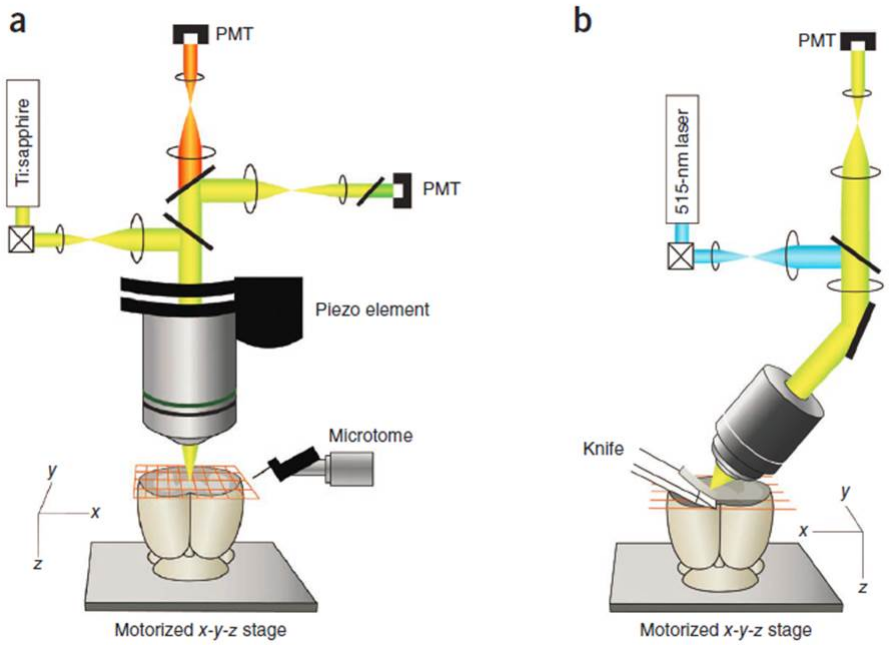

Figure 3.7: **Serial sectioning methods** (a) In STP tomography, a two-photon microscope is used to image the coronal plane of the mouse brain, afterwards a microtome sections off the imaged tissue. A piezo objective scanner can be used for z-stack imaging. (b) In fMOST, a confocal line-scan microscope is used to image 1-μm thin section of the brain previously cut by a diamond knife [41].

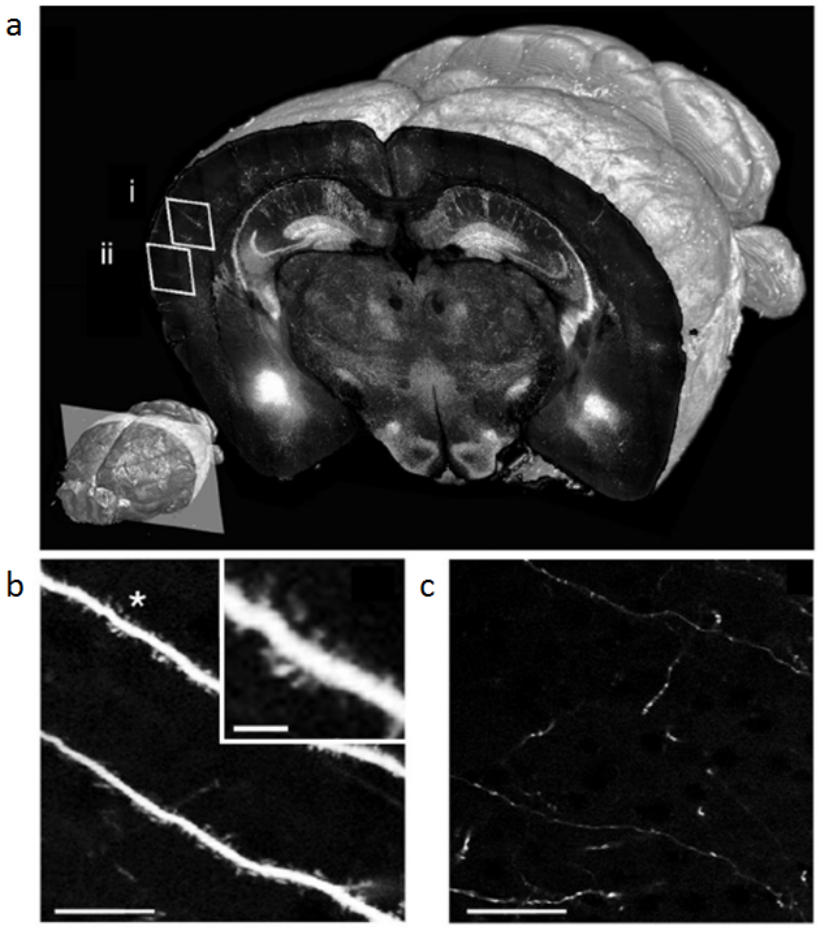

Figure 3.8: **STP tomography** (a) 3D view of a coronal section of the GFPM brain imaged with a 20× objective at 0.5 μm XY sampling. (b-c) Enlarged views from regions (i) and (ii) in panel, respectively, demonstrating visualization of dendritic spines and fine axon fibers; scale bar = 5 μm. Image taken from [14].

plane of the detection objective. The fluorescence emission is collected along an axis perpendicular to the illumination plane (figure 3.9). The optical paths of excitation and detection light are decoupled guaranteeing optical sectioning also with low-NA optics (axial resolution is given by the thickness of the light sheet). Moreover, with this approach, fluorophores are excited only at the focal plane of the detection objective, dramatically reducing the photobleaching compared to confocal microscopy.

The detection architecture is similar to the one of wide-field microscopy, making the acquisition faster compared with confocal and two-photon microscopy. Moving the sample through the light sheet permits to obtain a complete tomography of big specimens, such as whole mouse brains, in some hours. This technique drastically reduces acquisition time and achieves good resolution at high penetration depths. However, it requires the sample to be transparent. To allow imaging at high depths it is necessary to reduce light scattering and make the tissues transparent. This goal can be achieve homogenizing the refractive index inside and outside the sample by using clearing agents.

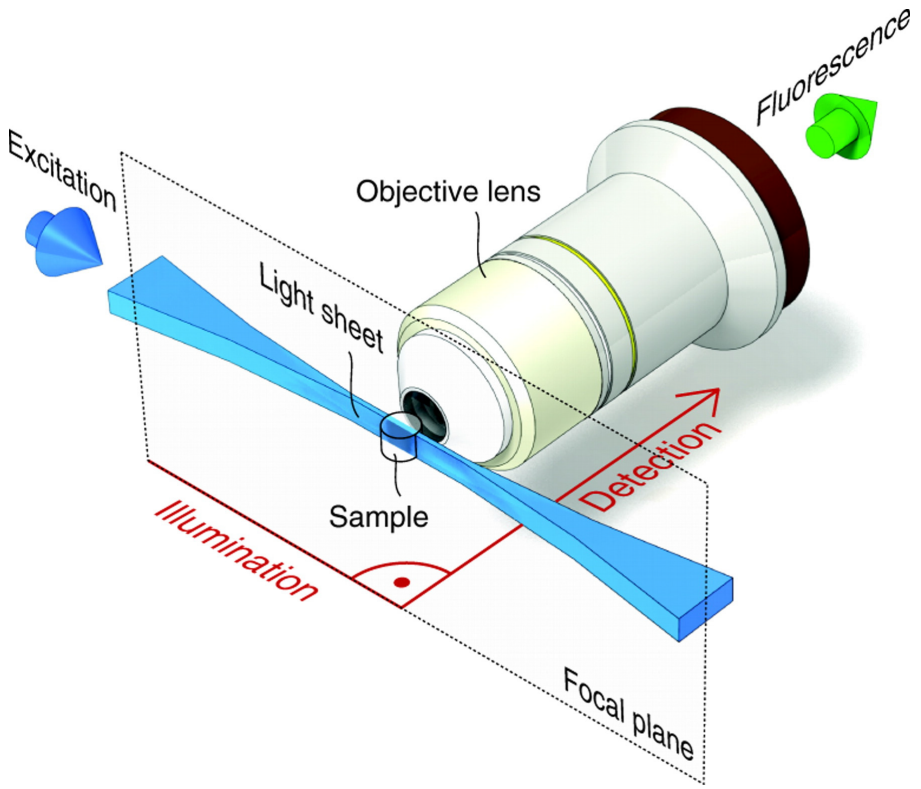

Figure 3.9: **Light sheet illumination microscope scheme** Excitation (in blue) and emission (in green) pathways are orthogonal to each other. The light sheet lies in the focal plane of the detection objective. Image taken from [42].

Chapter 4

Clearing methods

The inherent three-dimensional (3D) structure of cells and organs requires volumetric imaging. To investigate structure, different techniques, such as serial two-photon sectioning and light sheet microscopy, can be used. They allow 3D reconstruction of large specimens at high resolution, however, they are limited by light scattering. In fact, normally, light does not propagate well inside tissues because of scattering, making imaging of large tissue problematic. To improve imaging depth samples should be as transparent as possible. A large number of approaches have been developed that clear tissues to reduce scattering. This chapter describes the mechanism of light scattering and the clearing techniques that make tissues transparent and, therefore, are used for large volume 3D reconstruction.

4.1 Scattering and refractive index

Scattering is the event that occurs when the propagation of light rays deviate from their straight path when they encounter irregularities in the

propagating medium [44]. To clear samples is necessary to assure that all wavelengths pass "through" the tissue minimizing scattering. Scattering occurs when the refractive index between different regions of the sample is heterogeneous. In particular, this event limits the penetration of the light deep into the tissue when the variation of the refractive index is similar to the wavelength of the light used for imaging [45, 35, 46].

To reduce scattering and to make the tissue transparent, the refractive index has to be homogenized inside and outside the sample (figure 4.1). To this end different approaches have been developed based on organic solvents, aqueous solvents and tissue transformation.

4.2 Organic agents

Large tissue optical clearing was achieved for the first time by Spalteholz in 1914 [47] (table 4.1). His approach was based on two steps: a dehydration step (based on ethanol), that removes water from the tissue, and a clearing step with high refractive index organic solvents (benzylbenzoate and methylsalicilate), that achieves the final transparency. A drawback of this technique is the shrinkage of the tissue caused by the dehydration step. The diffusion of water is faster than the one of ethanol. Moreover, after clearing, the tissue is hard and difficult to cut and proteins fluorescence is not well preserved.

Subsequently, trying to preserve sample fluorescence, other clearing methods, based on the same principle, have been proposed. In 2007 Dodt et al. [16], used the combination of ethanol and BABB (benzylalcohol / benzylbenzoate) to perform three-dimensional visualization of neuronal networks in whole mouse brain with light sheet microscopy, yet fluorescence was maintained in the samples for only one day.

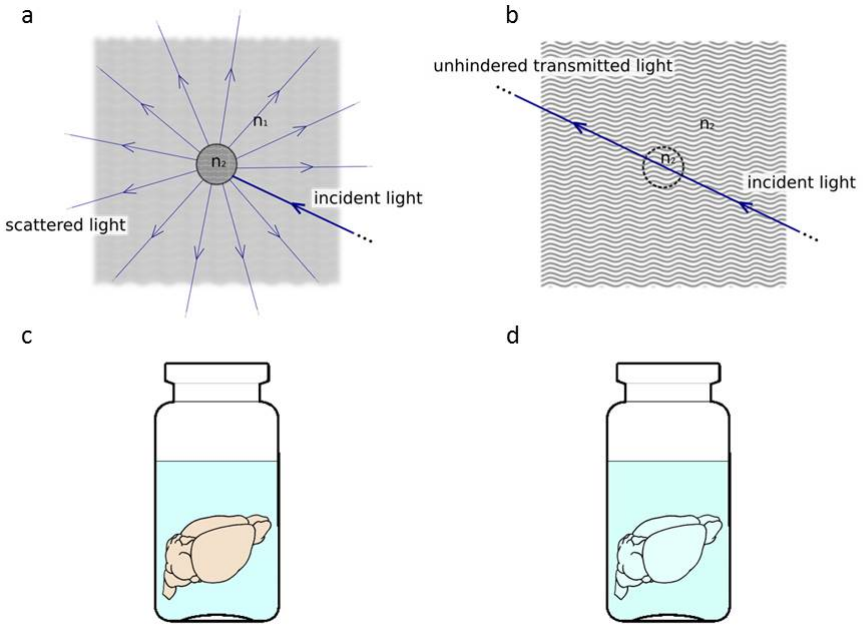

Figure 4.1: **Light scattering and refractive index matching** (a) Scattering occurs when the refractive index between different regions of the sample is heterogeneous ($n_1 \neq n_2$). (b) Scattering is strongly reduced and light can pass through the tissue when the sample and the surrounding medium have similar refractive indexes ($n_1 = n_2$). (c) and (d) Schematic drawing showing a brain before and after optical clearing.

Dehydration	Clearing	n	Transparency	Fluorescence	Ref
Ethanol	Benzylbenzoate	1.56	Yes	No	[47]
Ethanol	BABB	1.54	Yes	Yes/1day	[16]
THF	DBE	1.56	Yes	Yes/2days	[48]

Table 4.1: **Comparison between organic solvents based methods** The clearing is obtained in two steps: the first step of dehydration removes water from the tissue. Subsequently, the clearing step with high refractive index organic solvents achieves the final transparency. In the table there are the major agents used to clear mouse brains. BABB = benzyl alcohol / benzyl benzoate, THF = tetrahydrofurane and DBE = dibenzyl ether.

To prolong this time, Becker et al. in 2012 [48], tested different GFP-friendly dehydration and clearing solutions. They analyzed dehydration mediums such as ethanol, methanol, acetone, 2-butoxyethanol, dimethylformamide, dimethylsulfoxide (DMSO), tetrahydrofurane (THF) and dioxane, and clearing solution such as dibenzyl ether (n=1.56), methylsalicylate (n=1.51), benzyl alcohol (n=1.54), benzyl benzoate (n=1.56), transanethole (n=1.56), isoeugenol (n=1.57), isosafrol (n=1.57), 1,5- dibromopentane (n=1.51), and bromobenzene (n = 1.56). They concluded that the best clearing procedure, allowing fluorescence preservation up to two days, combines tetrahydrofurane (THF) and dibenzyl ether (DBE) (see figure 4.2), this technique was called 3DISCO [49]. Subsequently, the iDISCO method [50] combined the protocol with whole tissue immunostaing, avoiding the necessity of protein fluorescence preservation.

All these methods are used because they guarantee high transparency, they are easy to perform and very fast, and can be applied to different tissue types [16]. However, they have some disadvantages that limit their applicability. They lead to a fast protein fluorescence quenching (few days),

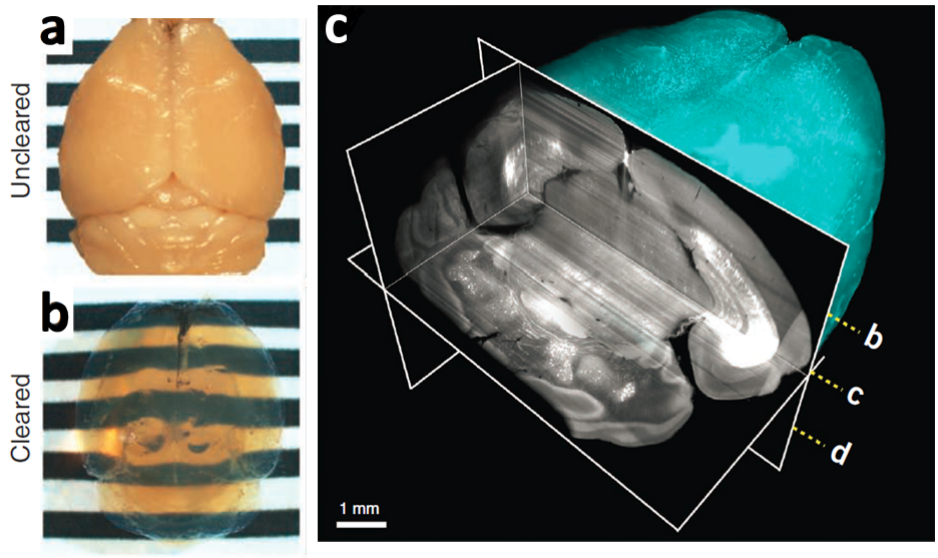

Figure 4.2: **3DISCO clearing** (a) (b) A mouse brain before and after 3DISCO clearing: the method achieves a high transparency. (c) The 3D reconstruction of a GFP-M mouse brain imaged with a light sheet microscope. Image modified from [49].

tissue alteration and shrinkage (sometimes of up to 50% [48]), moreover the majority of them have the capacity to dissolve glues used in the construction of objective lenses. For these reasons other approaches have been studied based on aqueous solutions.

4.3 Aqueous agents

The idea of using aqueous solutions for tissue clearing was born from the observation that dipping specimen in solution of glycerol and water (80% n = 1.44), routinely used for tissue mounting, leads also to sample clearing. This is true only for thin sample slices, but allows for the preservation of sample fluorescence. From this observation, to prevent protein fluorescence quenching, other approaches involving water-based optical clearing agents were developed. Among the first, there was the Sca*l*e procedure [51]. Sca*l*e utilizes urea for the hyper-hydration of the tissue. During the clearing step, urea can enter tightly folded regions of high refractive index proteins, creating an osmotic gradient that pulls water. This partially denatures proteins, hydrates them, and decreases the overall refractive index of the tissue. A similar approach was proposed in 2013: the Clear^T method [52]. It is based on a urea-like molecule (formamide) as active clearing reagent, which leads to hyper-hydration. Both of these techniques lead to fluorescence preservation, however, they lead also to massive tissue swelling and subcellular structure alterations (figure 4.3). Moreover, transparency is only achieved in tissue slides or in brain of newborn mice (up to 5 days) but not in the entire brain of adult mice.

Subsequently, another protocol based on the simple immersion of the tissue in a high refractive index aqueous solution was published, the SeeDB method [53]. It is based on saturated fructose solutions that achieve a $n =$

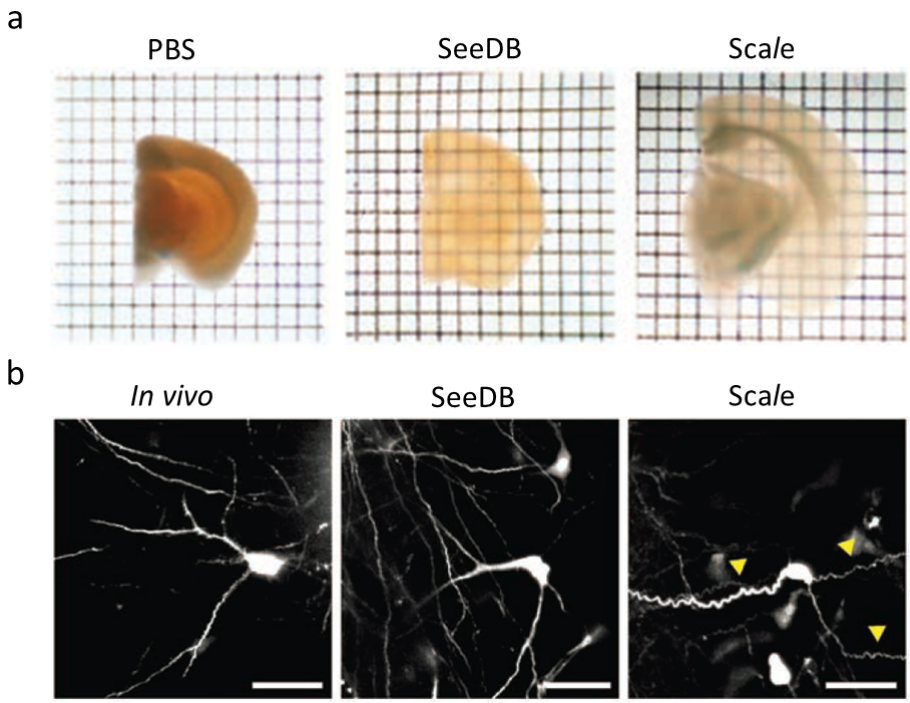

Figure 4.3: **Comparison between SeeDB and Sca*l*e clearing** (a) Adult 1.5 mm thick mouse brain slices before and after SeeDB and Sca*l*e clearing (transmission images). White matter is fully cleared with SeeDB, but not with Sca*l*e, moreover Sca*l*e produces a swelling of the tissue. (b) Image of neuron after clearing. In Sca*l*e-treated samples, it is possible to see morphological changes, dendrites appear serrated (yellow arrowheads), suggesting damages as a result of anisotropic sample volume changes. On the contrary, SeeDB-treated samples have a smooth appearance. Scale bars, 50 μm. Image modified from [53].

1.49. Fructose is not toxic, compatible with protein fluorescence and doesn't alter tissue structure (see figure 4.3). However, highly concentrated sugar solutions are difficult to manage due to their high viscosity and require long incubation times. Moreover, with this technique it is not possible to clear a whole adult mouse brain.

As a compromise between hyper-hydration and SeeDB other protocols were studied. The CUBIC method [54, 55], utilizes a hyper-hydration urea-based mechanism, but includes a high refractive index sucrose solution in the clearing process. However, to remove lipids and obtain transparent samples, it also uses very high levels of triton (50%) that result in protein loss (24%-41%), which lowers epitopes concentrations and weakens possible immunostaining. The same approach was used in the FRUIT techniques [56], that combine SeeDB and Sca*l*e techniques by mixing urea with fructose, and by the Sca*l*eS [57] that uses urea and sorbitol. Both lower the overall viscosity of the SeeDB fructose solution, however, they can't achieve whole mouse brain transparency.

Although aqueous techniques improve protein fluorescence preservation and are not toxic, they do not clear as well as the organic methods, limiting the quality of the acquired images.

4.4 Tissue transformation

Biological tissues, such as brain, are constituted by cells. Each cell compartment is bound by a membrane, consisting of a lipid bilayer. The lipid-aqueous interface contributes to creating heterogeneity in the refractive index and leads to light scattering. Moreover, these structures create a diffusion barrier that renders tissue poorly accessible to molecules. The penetration by chemicals and photons is fundamental in optical biology for

sample labeling and imaging.

Recently, based on these considerations, a new approach called CLARITY was developed [21, 58]. It addresses the challenge of producing large, transparent and fluorescently labeled volumes through tissue transformation. The method removes cell lipid bilayers and allows light and macromolecules to penetrate deep into the tissue, permitting three-dimensional imaging and immunohistological analysis. To provide structural integrity and retain biomolecules, CLARITY transforms the tissue into a nanoporous hydrogel-hybridized lipid-free form. The procedure is divided into four steps represented in figure 4.4.

The first step consists in the animal perfusion at 4°C with the hydrogel monomers (acrylamide and bisacrylamide), formaldehyde and the thermally triggered initiator. In this step, formaldehyde crosslinks the hydrogel monomers to biomolecules that have a reactive group (the amino group), such as proteins and nucleic acids.

The temperature is fundamental, in fact, in the second step, the polymerization of the biomolecule-conjugated monomers is triggered by increasing it. Tissue incubation at 37°C permits to obtain the hybridization of the tissue with the hydrogel. This construct physically supports tissue structure and chemically incorporates biomolecules. Importantly, lipids and biomolecules lacking functional groups for conjugation remain unbound and, therefore, can be removed.

Lipids extraction is carried out in the third step by electrophoretic tissue clearing (ETC). ETC is based on the active transport of ionic micelles through the tissue. Lipids are incorporated within micelles and removed from the specimen. The hydrogel is highly permeable, which allows immunohistochemistry, facilitating tissue labeling. As a final step, the refractive index matching solution FocusClear^{TM}, a very expensive solution, is

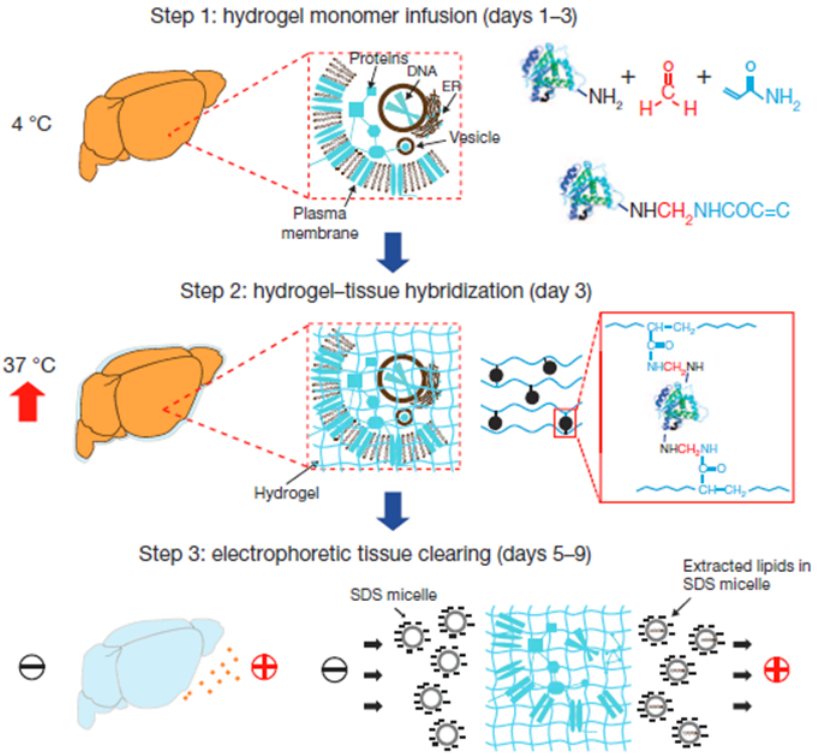

Figure 4.4: **CLARITY protocol** Scheme showing the different steps of the CLARITY method. The first step consists in the perfusion of the sample with formaldehyde and hydrogel monomers. The hydrogel-tissue hybridization occurs in the second step while in the third lipids are extract with an electrophoretic field. After that, the brain is ready for refractive-index matching and imaging. Reproduced from [21].

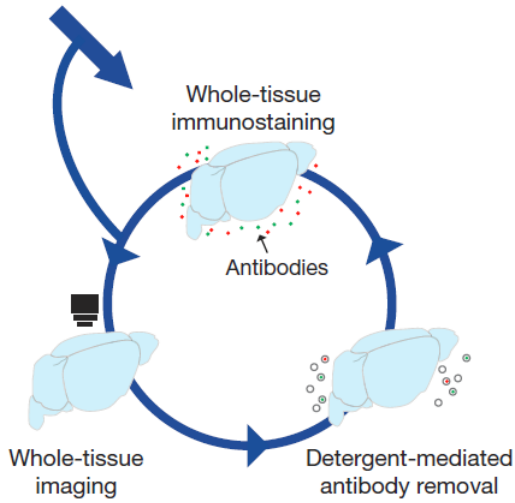

Figure 4.5: **Multiround immunostaining** CLARITY enables multiround molecular phenotyping. The permeability of clarified tissue facilitates rapid antibody exchange. Antibodies removal is performed with the ionic detergent used initially to create clarified tissue. The solution denatures antibodies and disrupts binding without structural damage or antigen degradation. After that new round of immunostaining can be performed. Reproduced from [21].

used to clear the sample. Imaging of cleared samples can be performed with any fluorescence microscopes. In the paper they used a confocal microscope (figure 4.6).

CLARITY is compatible with immunostaining. Indeed, without membrane lipids, antibodies can penetrate deep into tissue, allowing large brain tissue labeling. Chung et al. spread the applicability of this technique adding a multiround labeling that permits to analyze different epitopes of the same sample, opening the door for new approaches (figure 4.5 and 4.6).

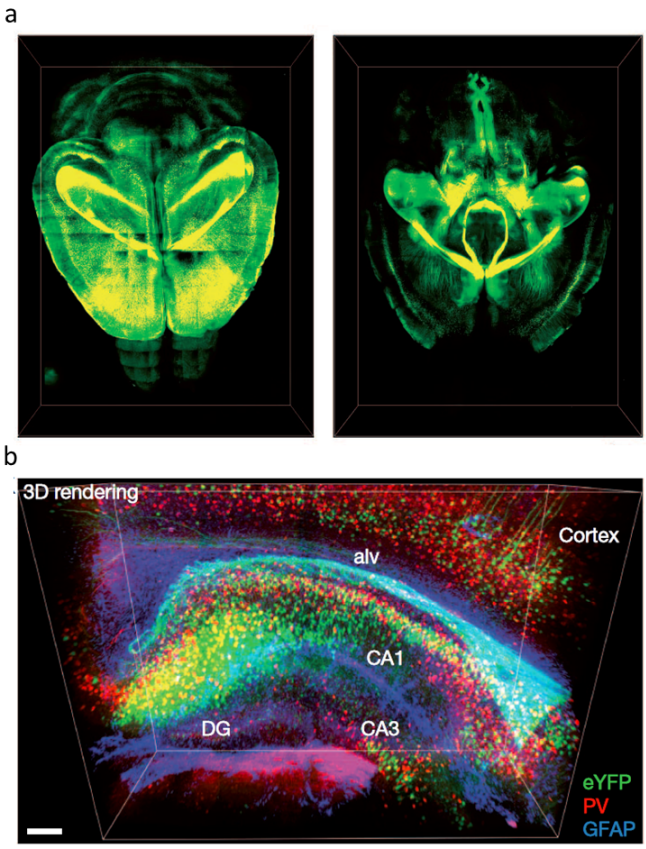

Figure 4.6: **Whole mouse brain imaging** (a) Images made with a confocal microscope of a Thy1-eYFP line-H mouse brain after CLARITY hydrogel-tissue hybridization, ETC, and refractive-index matching. (b) Three-dimensional view of mouse hippocampus showing eYFP expressing neurons (green), parvalbumin-positive neurons (PV, red) and astrocytes (GFAP, blue). Scale bar = 200 mm. Reproduced from [21].

However, CLARITY has some disadvantages. Focus Clear^{TM} is very expensive and that limits its practical applicability on routine experiments (e.g. since 1ml costs 20$, a whole mouse brain clearing can cost up to 2000$), moreover its composition is unknown due to patent protection.

Similar to this method, another technique called PACT (PAssive CLARITY Technique), that uses a Refractive Index Matching Solution (RIMS) to clear samples [59], was published. To achieve whole brain clearing and labeling they also developed PARS (Perfusion-assisted Agent Release in Situ) that delivered the PACT reagents perfusing animals. All of them are based on quick lipid removal and utilize a low-viscosity, high refractive index contrast reagent: the Histodenz, a diatrizoic acid based compound. As with the CLARITY protocol, also these methods require a long preparation time (weeks) and complicated procedures, but, in addition, they have the disadvantage of haven't been used for human brain analysis. Since, PACT derived from CLARITY and PARS needed to perfuse samples, in this work the CLARITY method was used as starting procedure to prepare mouse and human brain samples for both two-photon and light sheet imaging.

Part II

Methods

Chapter 5

Sample analysis: clearing and imaging techniques

As presented in the first part, to improve the imaging deep achievable with fluorescence microscopy it is necessary to make the tissue transparent. The present chapter provides an overview of the specimens used in this research, the protocols employed to make them clear and the fluorescence microscopy techniques used to image them.

5.1 Transgenic animal models

Different lines of transgenic mice were analyzed; for the sparse labeling of pyramidal neurons with GFP the Thy1-GFP-M line was used [60]. For the visualization of GABAergic interneurons GAD2-ires-Cre-tdTomato mice were used [61] and for imaging the subpopulation of parvalbumin-positive interneurons the PV-Cre-tdTomato line was used [62]. For the analysis of all Purkinje cells of the cerebellum the L7-GFP mice were used [63]. The

experimental protocols involving animals were designed in accordance with the laws of the Italian Ministry of Health.

5.2 Human brain specimen collection

Human brain samples were removed during a surgical procedure for the treatment of drug-resistant epilepsy in a child with hemimegalencephaly (HME). The sample was obtained after informed consent, according to the guidelines of the Human Research Ethics Committee of the A. Meyer Children's Hospital. Upon collection, the sample was placed in neutral buffered (pH 7.2-7.4) formalin (Diapath, Martinengo, Italy) and stored at room temperature.

5.3 Organic solvent clearing

This section describes the protocol used to prepare mouse brain samples for light sheet microscopy analysis. It is based on organic solvent clearing and consists in three step: sample fixation, clearing and imaging.

5.3.1 Preparation of PFA-fixed mouse brains

The following protocol was used to fix mouse brain samples before organic solvent clearing (with BABB and DBE). As described in the next section (5.4) it was used also for aqueous solution clearing (SeeDB and TDE).

Adult mice were deeply anesthetized with an intraperitoneal injection of ketamine (90 mg/kg) and xylazine (9 mg/kg). They were transcardially perfused with 100 ml of ice-cold 0.01 M phosphate buffered saline (PBS) solution (pH 7.6), followed by 100 ml of freshly prepared ice-cold paraformaldehyde (PFA) 4% in 0.01 M PBS (pH 7.6).

The brain was extracted from the skull and fixed overnight in 20 ml of PFA 4% at 4°C. Samples were then rinsed three times (30 minutes each) in 20 ml of 0.01M PBS at 4°C. The brains were stored in 20 ml of 0.01M PBS at 4°C.

For transmission electron microscopy (TEM) the anesthetized animal was perfused with 10 ml of PBS immediately followed by 300 ml of a mixture of 2.5% glutaraldehyde (Glut) and 2% PFA in 0.01 M phosphate buffer (pH 7.4). After 2 hours, the brain was removed and stored at 4°C in 50 ml of 0.01M PBS.

5.3.2 Organic solvent optical clearing

Optical clearing of murine PFA-fixed brains with organic solvents was performed in two steps: the dehydration and the clearing step (see figure 5.1). The dehydration step was performed either with ethanol or tetrahydrofuran (THF). The clearing was achieved with benzyl alcohol/benzyl benzoate (BABB) or dibenzyl ether (DBE) following the protocol of Dodt et al. [16] and Becker et al. [48].

Dehydration was achieved with serial incubation in 20 ml (vol/vol) solutions of ethanol/water or THF/water 50%, 70%, 80%, 90%, 96%, 100% for 1 hour each, then 100% overnight. Incubations were made on a rotating wheel at room temperature (RT).

For clearing the sample was put in 20 ml of 100% BABB (1 part of benzyl alcohol and 2 parts of benzyl benzoate) or 100% DBE for 1 day at RT while rotating (the solution is changed at least 1 time during the incubation).

THF, BABB and DBE solutions can carry peroxides that destroy protein folding and lead to fluorescence bleaching. To avoid it, peroxides were

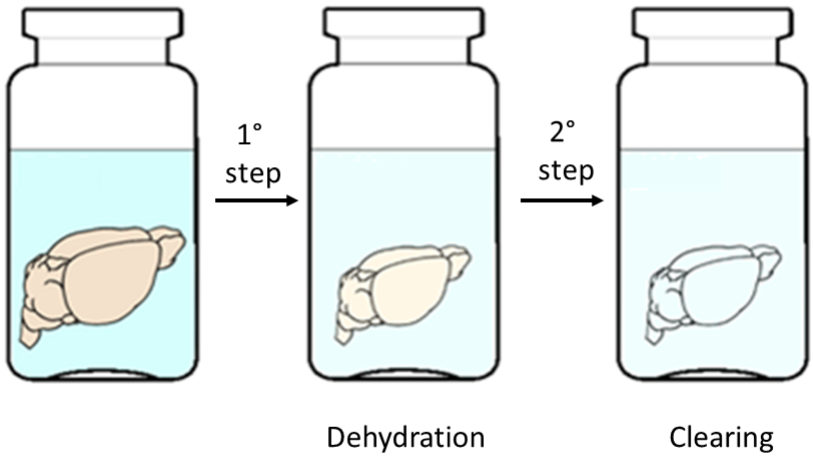

Figure 5.1: **Organic solvent clearing** The approach is based on two steps: a dehydration step, that removes water from the tissue, and a clearing step with high refractive index organic solvents, that achieves the final transparency. Image modified from [64].

removed from solutions with an aluminum oxide filtration (250 g of alumin oxide per liter, see figure 5.2) before the clearing procedure.

Peroxide filtration in THF leads to the removing of THF stabilizer. This stabilizer is required to prevent THF explosion. Therefore, it is substituted by adding 250 mg/l butyl hydroxyltoluol (BHT) into the receiver flask.

5.3.3 Imaging with light-sheet microscopy

Specimens were imaged using a custom-made light sheet microscope (LSM) described in Silvestri et al [65]. Briefly, in this LSM the light sheet is generated using a laser beam scanned by a galvanometric mirror (VM2500+, Cambridge Technology); a de-scanning system in the detection path creates a fixed image of the excitation scanning line in a secondary image plane, where a linear spatial filter (slit, p/n 35290NR, JML Optical) is positioned. A third scanning system reproduces a wide-field-like image on the chip of an EMCCD camera (Cascade II: 512, Photometrics). The laser light was provided by a diode laser (Excelsior 488, Spectra Physics), $\lambda = 488$ nm. An acoustic-optic tunable filter (AOTFnC-400.650-TN, AA Opto-Electronic) was used to regulate laser power. The sample was mounted on a tipped plate and placed in a custom-made chamber which allowed brain tissue being immersed in clearing solution during imaging. A motorized stage allowed 3D motion of the sample, as well as rotation around the vertical axis (three M-122.2DD and one M-116.DG, Physik Instrumente). An achromatic doublet (CVI Melles Griot, focal length 50 mm) was used for illumination, while the objective lens used for detection was a 20× Nikon Plan SLWD (NA 0.35, WD 24 mm). The slit aperture was set to 15 μm.

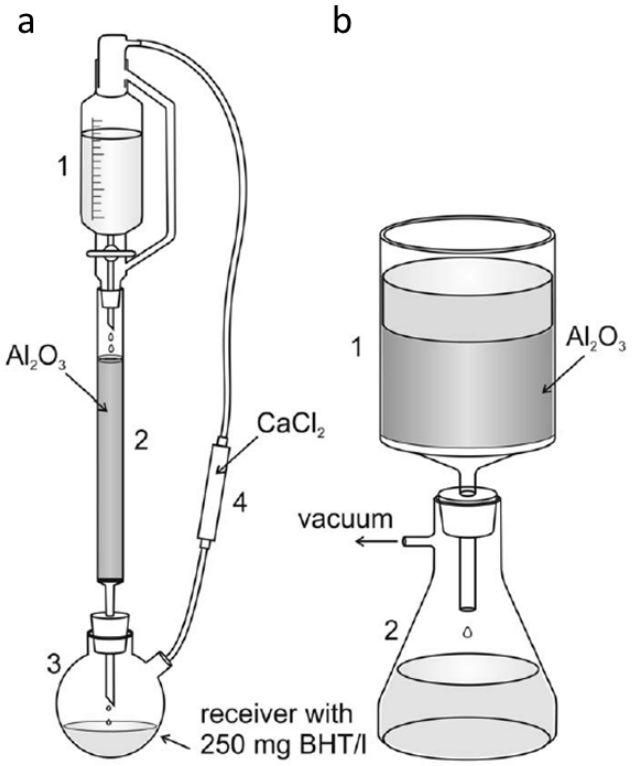

Figure 5.2: **THF, BABB and DBE filtration** (a) Scheme showing the apparatus for THF peroxide removal. Since THF is volatile the system is closed. The solution is placed in a dropping funnel with pressure compensation (1). A chromatography column filled with aluminum oxide filters the solution (2) that is collected in a round bottom flask (3). A drying tube (4), filled with calcium chloride, absorbs water vapor. (b) Scheme showing the apparatus for BABB and DBE peroxide removal. The filter unit (1) consists of aluminum oxide powder and filter paper (16-40 μm pore size). A vacuum tight filtering flask collects the solution after filtration (2). Image taken from [48]

5.4 TDE clearing for two-photon imaging

TDE can be used directly on PFA-fixed sample. This clearing protocol combined with serial two-photon sectioning allowed for the reconstruction of large samples. This section describes the two-photon fluorescence microscope used for the characterization of TDE direct clearing and analyzes the system to perform serial two-photon tomography.

5.4.1 Direct TDE clearing

Mouse brain samples were perfused with PFA as described in 5.3.1, then they were cleared with serial incubations in 20 ml of 20% and 47% (vol/vol) 2,2'-thiodiethanol in 0.01M PBS (TDE/PBS), each for either 1 hour at 37°C or for 12 hours at room temperature (RT) while gently shaking. After clearing they were ready to be imaged.

5.4.2 Two-photon fluorescence microscopy

The custom-made two-photon fluorescence microscope (TPFM) (figure 5.3, described in [66]) was constituted by a mode locked Ti:Sapphire laser (Chameleon, 120 fs pulse width, 80 MHz repetition rate, Coherent, CA) coupled into a custom-made scanning system based on a pair of galvanometric mirrors (VM500+, Cambridge Technologies, MA). The laser was focused into the specimen by a water immersion 20× objective lens (XLUM 20, NA 0.95, WD 2mm, Olympus, Japan) for uncleared (PBS) sample imaging or a tunable 20× objective lens (Sca*l*e LD SC Plan-Apochromat, NA 1, WD 5.6mm, Zeiss, Germany) and a tunable 25× objective lens (LD LCI Plan-Apochromat, NA 0.8, WD 0.55mm, Imm Corr DIC M27, Zeiss, Germany) for cleared (47% TDE/PBS) sample imaging. The system was

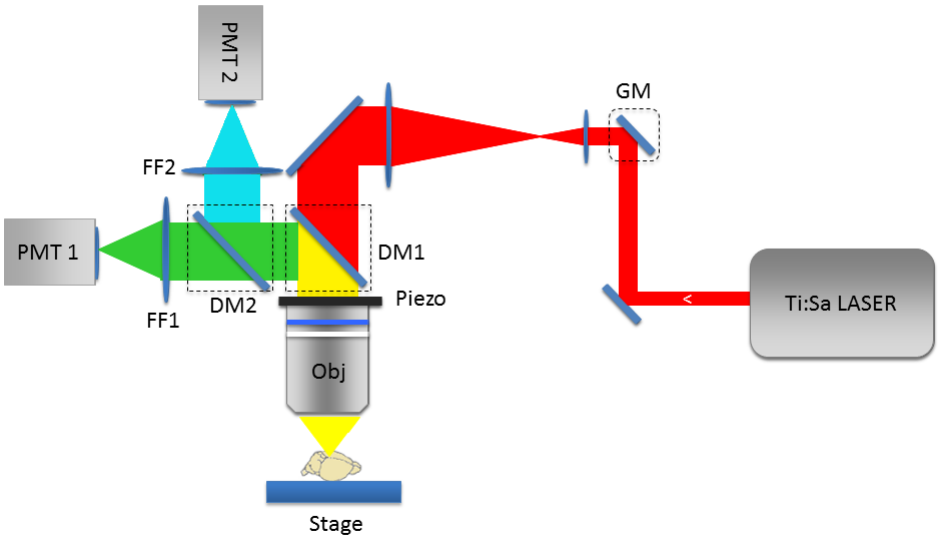

Figure 5.3: **Two-photon fluorescence microscope (TPFM)** Simplified scheme showing the TPFM apparatus. Obj = objective, GM =galvanometric mirror, DM =dichroic mirror, FF = fuorescence filter, PMT = photomultiplier tube, Piezo = piezoelectric stage. Two-photon excitation light is in red while fuorescence emission is in green and cyan. Image modified from [66].

equipped with a motorized xy stage (MPC-200, Sutter Instrumente, CA) for lateral displacement of the sample and with a closed-loop piezoelectric stage (ND72Z2LAQ PIFOC objective scanning system, 2mm travel range, Physik Instrumente, Germany) for the displacement of the objective along the z axis. The fluorescent light is separated from the laser optical path by a dichroic beam splitter (DM1) positioned as close as possible to the objective lens (non-de-scanning mode). A two-photon fluorescence cut-off filter (720 SP) eliminates reflected laser light. A second dichroic mirror (DM2) is used to split the two spectral components of the fluorescence signal. The fluorescence signals are filtered with 630/69 and 510/42 filters (FF1 and FF2) and collected by two orthogonal photomultiplier modules (H7422P, Hamamatsu Photonics, Japan). The instrument was controlled by custom software, written in LabView (National Instruments, TX).

5.4.3 Serial two-photon tomography

The two-photon fluorescence microscope was coupled with a vibratome (Vibratome 1000 Plus, Intracel LTD, UK) to perform a serial two-photon tomography of a Thy1-GFP-M hippocampus. The hippocampus was manually dissected from a PFA-fixed adult (p56) mouse brain and cleared by two serial incubations in 20 ml of 20% and 47% (vol/vol) TDE/PBS, each for 1 hour at 37°C while gently shaking. After clearing, the hippocampus was embedded in a solution of 47% TDE/PBS (vol/vol) - agar 4% (wt/vol). In order to reduce the number of slices required, the hippocampus was horizontally oriented with respect to the optical planes acquired. Serial sectioning was performed with the vibratome and after every cut the sample was left in 47% TDE/PBS overnight at RT. Stacks of each layer were acquired with the TPFM (Zeiss 20× Scale objective, pixels size 0.59 × 0.59 μm^2) using

a custom LabView program (National Instruments) allowing for automatic acquisition of adjacent regions drawing a spiral square. Each stack had a depth of 1000 μm with a z displacement of 4 μm between images. Each frame had a field of view of 300 $\times$ 300 μm^2, adjacent stacks had an overlap of 30 μm. To ensure an efficient 3D reconstruction along the z axis, slicing was performed every 800 μm such that the subsequent layer had an overlapping region of 200 μm with the previous one. To obtain constant fluorescence intensity, laser power was increased during acquisition according to the imaging depth, however, some illumination inhomogeneity were present due to the inherent heterogeneity of the tissue.

5.5 CLARITY - TDE clearing for light sheet microscopy

To perform light sheet microscopy, TDE clearing was combined with the CLARITY method. This section describes the protocol used to prepare mouse brain samples for LSM analysis. It consists of different steps: CLARITY fixation, sample labeling, TDE clearing and LSM imaging.

5.5.1 Preparation of CLARITY-processed mouse brains

CLARITY mouse brains were prepared according to the Chung protocol (figure 4.4) [21]. Samples were then cleared with either FocusClear^{TM} or TDE allowing LSM imaging.

Adult mice were anaesthetized with isofluorane and transcardially perfused with 20 ml ice-cold PBS solution (pH 7.6) followed by 20 ml of a mixture of 4% (wt/vol) PFA, 4% (wt/vol) acrylamide, 0.05% (wt/vol) bis-acrylamide, 0.25% (wt/vol) VA044 in PBS.

Brains were extracted and incubated in the same solution at 4°C for 3 days. The samples were then degassed and the temperature was increased to 37°C to initiate polymerization. The embedded sample was extracted from the gel and washed with clearing solution at 37°C through gentle shaking.

To perform electrophoretic tissue clearing (ETC), hydrogel-embedded brains were placed in a custom-built organ-electrophoresis chamber (see figure 5.4). Sodium borate buffer (200 mM, pH 8.5) containing 4% (wt/vol) sodium dodecyl sulfate (SDS) was circulated through the chamber and a voltage of 20V was applied across the ETC chamber at 37°C for several days.

After clearing, brains were incubated in $PBST_{0.1}$ (PBS and 0.1% Triton X-100, pH 7.6) at 37°C for 2 days to remove the SDS.

For vasculature staining, a specialized CLARITY perfusion protocol was applied. It was developed in collaboration with J.P Ghobril from the Laboratory of Neural Microcircuitry, Brain Mind Institute, EPFL, Lausanne, Switzerland.

Mice were anesthetized with pentobarbital (150 mg/kg) and transcardially perfused with PBS and 10ml of CLARITY monomer solution. After this, a third perfusion was performed with 20 ml of the monomeric solution containing FITC-albumin at 4mg/ml.

During polymerization the fluorescent albumin tightly integrated into the acrylamide mesh and was therefore not eliminated during lipid removal.

5.5.2 Sample labeling and optical clearing

Mouse brain samples treated with CLARITY were optically cleared with serial incubations in 50 ml of 30% and 63% (vol/vol) 2,2'-thiodiethanol in 0.01M PBS (TDE/PBS), each for 1 day at 37°C while gently shaking before

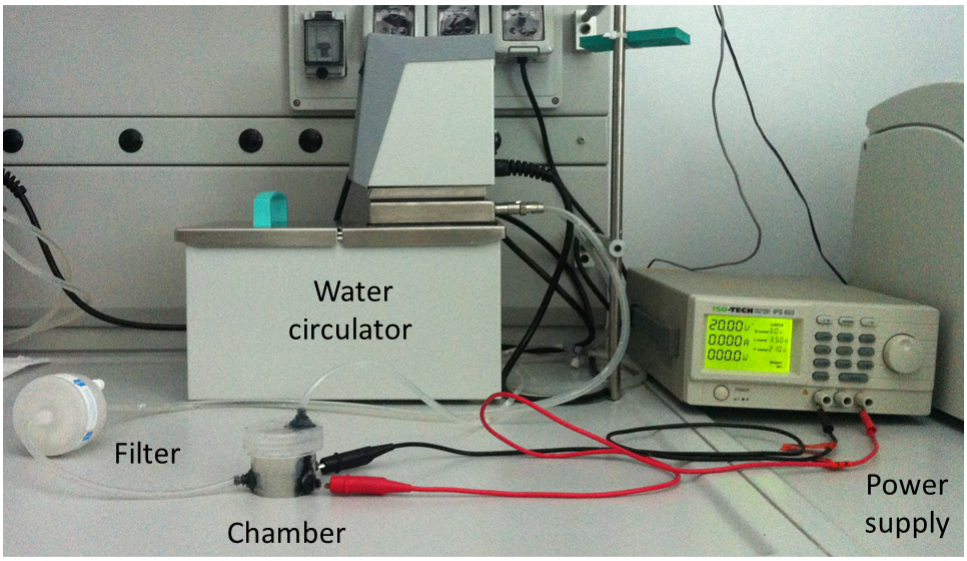

Figure 5.4: **CLARITY-ETC apparatus** Photo of the custom-made electrophoresis apparatus. The sample is placed inside a plastic chamber, lipids are extracted from tissue with an electric field created by a power supply. Electrodes (made with platinum wires) are placed inside the chamber on sides and are linked with the power supply, negative and positive wires are respectively black and red. The clearing solution flow is controlled by the temperature controlled water circulator that is set at 37°C. The solution before entering again in the chamber passes trough a filter for lipid removal.

imaging with a light sheet microscope.

For whole brain nuclei staining, CLARITY-processed murine samples were incubated at 37°C for 2 days with 1:50 Propidium Iodide (PI, LifeTechnologies, CA, P3566) solution, in $PBST_{0.1}$ followed by washing at 37°C for 1 day in $PBST_{0.1}$ solution.

5.5.3 TDE-CLARITY sample imaging with light-sheet microscopy

Specimens were imaged using a custom-made light sheet microscope (LSM) described in Müllenbroich et al. [67] (see figure 5.5). The light sheet was generated by scanning the excitation beam with a galvanometric mirror (6220H, Cambridge Technology, MA) and confocality was achieved by synchronizing the galvo scanner with the line read-out of the sCMOS camera (Orca Flash 4.0, Hamamatsu Photonics, Japan). Five different wavelengths were available (MLDs and DPSSs, Cobolt, Sweden) for fluorescence excitation and an acousto-optic tunable filter (AOTFnC-400.650-TN, AA Opto-Electronic, France) was used to regulate laser power. The excitation light was focused with a long working distance, low magnification objective (10×, 0.3 NA, WD 17.5mm, Nikon, Japan) and fluorescence was collected on a perpendicular axis with a specialized objective for high refractive index immersion solutions with a correction collar for refractive indexes ranging from 1.41 to 1.52: the 25× Olympus objective (XLSLPLN25XGMP, 25×, 1.0 NA, WD 8mm Olympus, Japan). The samples were mounted on a motorized x-, y-, z-, ϕ -stage (M-122.2DD and M-116.DG, Physik Instrumente, Germany) which allowed free 3D motion plus rotation in a custom-made chamber filled with 63% TDE/PBS. The microscope was controlled via custom written LabVIEW code (National Instruments) using the Murmex package

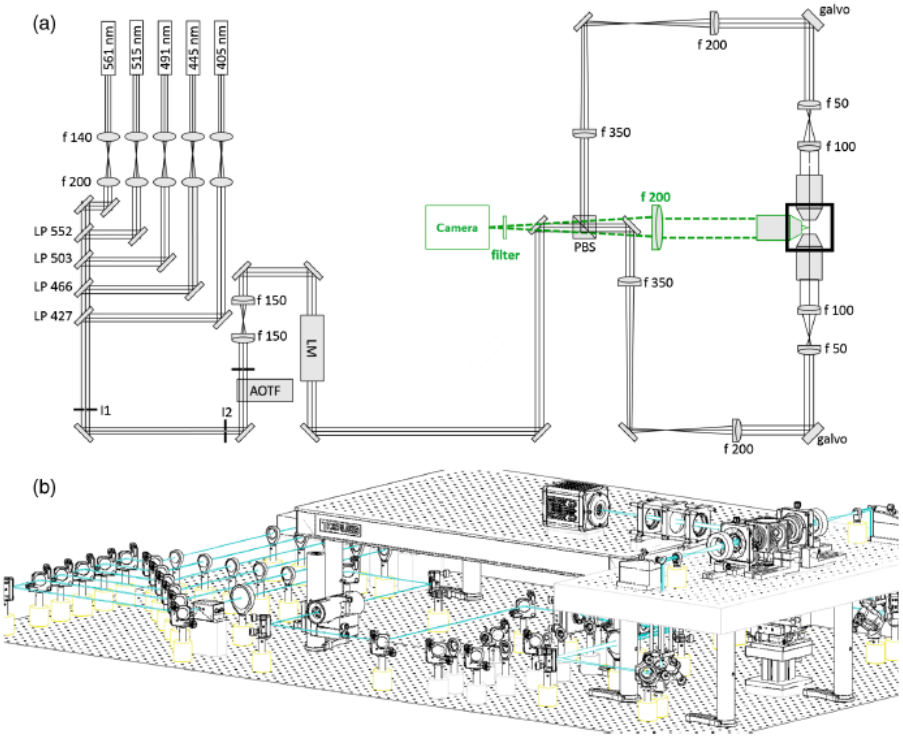

Figure 5.5: **Light sheet microscope (LSM)** Simplified scheme showing the LSM apparatus. (a) Scheme of the light path. LP: long-pass filter, I: iris, AOTF: acousto-optical tunable filter, LM: laser modulator, PBS: polarization beam splitter. Green dotted: detection path. (b) Oblique view of the microscope. Image taken from [67].

(Distrio, The Nederlands) which coordinated the galvo scanners, the rolling shutter and the stack acquisition.

5.6 TDE passive CLARITY methods for human brain analysis

For translational analysis, a passive CLARITY (PC) protocol was optimized using Chung et al. [21] as a starting point. It was used in combination with an immunohistochemistry protocol and TDE clearing. This method allowed sample imaging with two-photon fluorescence microscopy described in 5.4.2. This section describes the preparation of the sample, the staining and the clearing. The PC protocol has been applied to Thy1-GFP-M mouse brain slices and a human brain bioptic sample.

5.6.1 Preparation of passive CLARITY samples

Blocks of fixed samples were washed in PBS at 4°C for one day and then incubated in 4% (wt/vol) PFA, 4% (wt/vol) acrylamide, 0.25% (wt/vol) VA044 in PBS at 4°C for 2 weeks.

Samples were degassed and then the temperature was increased to 37°C to initiate polymerization. The embedded samples were extracted from the gel and incubated in clearing solution (sodium borate buffer 200 mM, pH 8.5) containing 4% (wt/vol SDS) at 37°C for two weeks while gently shaking. After lipids removal, samples were incubated in $PBST_{0.1}$ at 37°C for 1 day to remove the SDS.

Before staining, human CLARITY brain samples were manually cut into pieces of approximately 2 mm^3 using a scalpel.

5.6.2 Staining and clearing of PC-processed samples

To perform immunostaining, PC processed samples were incubated at RT for 2 days with the primary antibody (dilution, 1:50) in $PBST_{0.1}$ solution, followed by washing at RT for 1 day in $PBST_{0.1}$ solution.

The tissue was then incubated with the secondary antibody (dilution, 1:50-1:100) at RT for 2 days in $PBST_{0.1}$ solution, followed by washing at RT for 1 day in $PBST_{0.1}$ solution.

As primary antibodies an anti-PV (parvalbumin) antibody (Abcam, UK, cat. ab11427 or ab64555) and an anti-GFAP (glial fibrillary acidic protein) antibody (Abcam, cat. ab53554) were used and as secondary antibody the Alexa Fluor 568 conjugated IgG (Abcam, cat. ab175471 or ab175704) and the Alexa Fluor 488 conjugated IgG (Abcam, cat. ab150105) were used.

After staining, samples were optically cleared with serial incubations in 10 ml of 20% and 47% TDE/PBS for 10 minutes at 37°C while gently shaking and imaged with the two-photon fluorescence microscope (described in 5.4.2) using two color channels .

5.7 Image processing and data analysis

Light sheet fluorescence microscopy and serial two-photon tomography allow the reconstruction of large samples at high resolution. During acquisition a large number of data are produced.

The Terastitcher [68] tools was used to achieve a 3D image of whole specimens from raw data. This is a stitching tool capable of dealing with teravoxel-sized images. In collaboration with Leonardo Onofri and Giulio Iannello (Department of Engineering, University Campus Bio-Medico of Rome, Italy) it was used to process data acquired with both light sheet

microscopy and two-photon fluorescence microscopy. Moreover, it was adjusted to analyze data acquired through serial two-photon sectioning and was modified for double channel recording for the immunostaining images analysis.

Graphs and data analysis were done with OriginPro 9.0 (OriginLab Corporation). Image stacks were analyzed using both Fiji (http://fiji.sc/Fiji) and Amira 5.3 (Visage Imaging) software. 3D renderings of stitched images were produced using the Amira Voltex function. The Filament Editor of Amira was used to trace manually neuronal filaments.

Chapter 6

Characterization of the TDE clearing method

The major result of this thesis is the development of a new clearing method for multi-modal brain imaging, based on the aqueous agent 2,2'-thiodiethanol (TDE). This chapter presents the techniques used to validate this new approach.

6.1 Measurement of light transmittance and linear deformation

Light transmittance was determined using a spectrophotometer (Lambda 950 UV/Vis/NIR Perkin Elmer, MA) with uncleared slices in PBS as reference samples. Specimens were processed as follow.

PFA-fixed Thy1-GFP-M mouse brains were embedded in 4% agarose in 0.01 M PBS and cut into 1 mm coronal sections with a vibratome. The agarose surrounding each half-brain slice was removed and the slices were

cleared by serial incubations in 20%, 47%, 60%, 80% and 100% (vol/vol) TDE/PBS, each for 1 hour in 20 ml glass vials at 37°C while gently shaking.

Clearing with SeeDB was performed following the protocol described by Ke et al [53]. Slices were cleared by serial incubation in 20 ml of 20%, 40% and 60% (wt/vol) fructose, each for 4-8 hours and incubated in 80% (wt/vol) fructose for 12 hours, 100% (wt/vol) fructose for 12 hours and finally in SeeDB (80.2% wt/wt fructose) for 24 hours while gently rotating at RT.

For CLARITY mouse brains, a different protocol for sample preparation was followed. Since the porosity of the final gel makes samples unsuitable for agarose embedding and vibratome cutting, 2 mm thick coronal slices were obtained from a Thy1-GFP-M mouse CLARITY brain using a rat brain slicer (Alto rat brain coronal matrices, CellPoint Scientific, MD). Slices were then cleared by serial incubations in 20 ml of 20%, 47%, 63% (vol/vol) TDE/PBS, each for 1 hour at 37°C while gently shaking or with FocusClear^{TM} (CelExplorer Labs, Taiwan).

For the evaluation of linear deformation, sample photos were taken on a glass dish filled with PBS or the respective clearing mediums. Images of whole CLARITY mouse brains were taken with a stereomicroscope after 1 day incubation for each solution of TDE/PBS or after 3 days incubation in FocusClear^{TM}. Based on top view photos, the area of the samples was determined using ImageJ/Fiji. The linear deformation was quantified by normalizing the area of the cleared brain with the area of the brain in PBS and calculating the square root of that quotient. To characterize possible nonlinear distortion the edges of brain slices or whole brain were manually traced using GIMP (www.gimp.org), resized using the linear deformation parameter obtained before, and superimposed using different colors.

6.2 Measurement of protein fluorescence quenching and bleaching

GFP fluorescence quenching and bleaching evaluation were performed on uncleared and cleared, PFA-fixed samples imaged with TPFM. Fixed Thy1-GFP-M mouse brain slices of 2 mm thickness were optically cleared with 47% TDE/PBS at 37°C. To measure the effect of quenching two-photon images were acquired at different times and slices were incubated in 47% TDE/PBS at RT between acquisitions. Freshly made TDE solution was used for every measurement. The mean fluorescence intensity of homogeneous regions ($100 \times 100\ \mu m^2$ region of interest; ROI) was measured for each time point using ImageJ/Fiji. Bleaching was quantified as the temporal decay of the mean fluorescence intensity in a ROI enclosing a dendrite portion ($20 \times 20\ \mu$m2) and the value of a neighboring area without a dendrite was subtracted as background.

6.3 Evaluation of imaging depth

A brain slice of 2 mm thickness, from a wide-type (FVB) mouse, was incubated in $PBST_{0.5}$ (PBS and 0.5% triton X-100, pH 7.6) for 2 hours at RT while gently shaking. Slices were then stained with 10 μM DAPI (4',6-Diamidino-2-Phenylindole, Dihydrochloride, LifeTechnologies, CA, D1306) in 3 ml $PBST_{0.1}$. To compare the achievable imaging depth before and after clearing with 47% TDE/PBS, stacks of 600 μm depth with a z step of 2 μm were acquired with TPFM. Then imaging depth was quantified by the decay of the image contrast value with depth in cleared and uncleared samples. The image contrast of each frame was calculated with the following equation.

$$Contrast = \sqrt{\frac{\sum_i (c_i \times (i - \overline{I})^2)}{C - 1}} \tag{6.1}$$

Where c_i is the pixel count for intensity level i in an image (with i ranging between gray levels 0 and 255). $\overline{I} = I/C$ is the average intensity of the image with I defined as the image intensity integral $I = \sum_i i \times c_i$ and C as the total pixel count $C = \sum_i c_i$ [69].

6.4 Transmission electron microscopy

Using a vibratome (Vibratome 1000 Plus, Intracel LTD, UK), sections of 500 μm thickness were cut from a Thy1-GFP-M Glut-PFA-fixed mouse brain (the fixation protocol is described in 5.3.1). Slices were incubated in PBS or in 47% TDE/PBS for 4 days at 37°C while gently shaking. Samples were washed with 50 ml of 0.01M PBS for 30 minutes and 3 times for 5 minutes each in 20 ml of 0.1 M cacodylate buffer (pH 7.4). Post-fixation, en-bloc staining and resin embedding for transmission electron microscopy sectioning and imaging were performed following Knott et al [70]. A fixation of 40 minutes with 1% osmium tetroxide in 0.1M cacodylate buffer (pH 7.4) was performed at RT. Sections were then washed twice for 5 minutes in distillated water followed by 10 minutes of 1% aqueous uranyl acetate. Sections were dehydrated in graded alcohol series (2×50%, 1×70%, 1×90%, 1×95%, 2×100%) for 3 minutes each with a final step of 10 minutes in propylene oxide. Sections were then embedded in EPON through an incubation of 1 hour in 1:1 propylene oxide:EPON, two incubations of 30 minutes in 100% EPON and one incubation of 4 hours in fresh 100% EPON. Finally, sections were placed in fresh EPON and incubated for 24 hours at 65°C to allow resin polymerization. Images were obtained with a TEM microscope

(TEM CM 12, PHILIPS).

6.5 Hematoxylin and eosin staining

For anatomopathological characterization, formalin fixed paraffin embedded sections from the clinical resection specimens were stained with hematoxylin and eosin according to standard methods. To deparaffinize and rehydrate samples, the sections were placed in a slide holder and incubated in a solution of xylene (three minutes for three times) than in ethanol 100% (3min for 3 times), 95%and 80% 3min for 1 time, finally in deionized H_2O for five minutes. Hematoxylin staining was performed with an incubation of three minutes, than the sample was rinsed with deionized water following by tap water (five minutes). Destaining of not specific labeling was done with acid ethanol followed by tap water and deionized water washing. Subsequently eosin staining was performed for 30 seconds, then dehydration with 95% and 100% ethanol and xylene (three times for five minutes each) allowing the final fixation with a coverslip and Permount.

Part III

Results

Chapter 7

Characterization of clearing agents

In the last few years, different clearing approaches have been proposed to permit the investigation of microscopic anatomical details over whole excised organs. The purpose of this thesis is to characterize the major clearing techniques present in literature and evaluate a new method for multi-modal brain imaging. This chapter will present the results obtained using both organic and aqueous solvents for brain tissue clearing.

7.1 Organic solvent clearing

Based on literature, the organic clearing methods tested in this thesis were ethanol in combination with benzyl alcohol / benzyl benzoate (BABB, Dodt et al. [16]) and tetrahydrofuran (THF) with dibenzyl ether (DBE, Becker et al. [48] also called the 3DISCO method [49]).

Two parameters were used to evaluate the capabilities of the techniques:

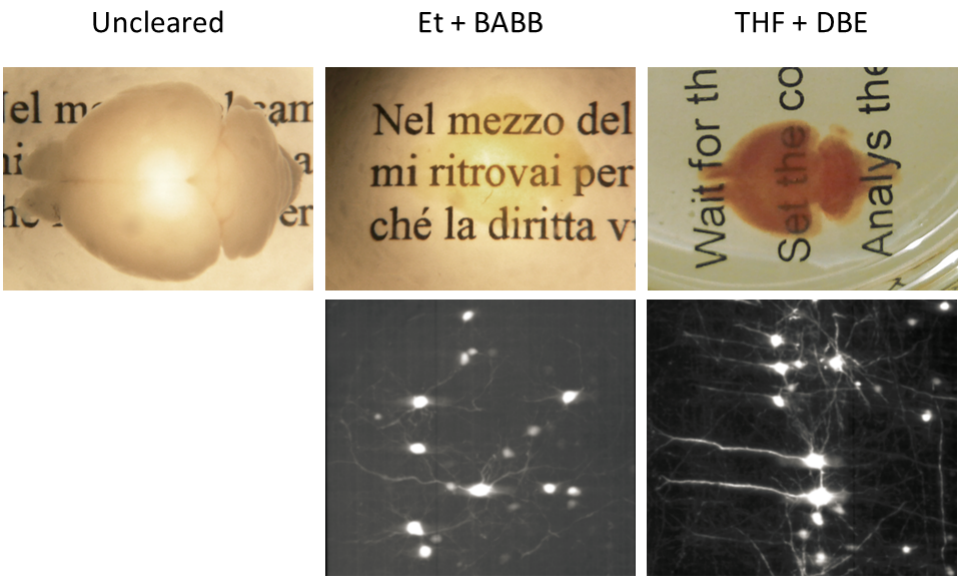

Figure 7.1: **Comparison between organic clearing** Thy1-GFP-M mouse brains uncleared and cleared with ethanol (Et) and benzyl alcohol / benzyl benzoate (BABB), and tetrahydrofuran (THF) in combination with dibenzyl ether (DBE). The transparency achievable with both techniques is comparable, on the contrary, the protein fluorescence is better preserved in the second method leading to a better contrast.

the transparency achievable and the fluorescence protein preservation. As shown in figure 7.1 both the techniques reach good transparency.

It is possible to notice some tissue browning, but it doesn't affect measures significantly. On the contrary, it is possible to observe a different protein fluorescence preservation between the two techniques. Ethanol and BABB damaged protein fluorescence resulting in lower fluorescence intensity and a high background noise. The contrast is better using THF and

DBE as shown in figure 7.1.

The good transparency and contrast achievable with the THF/DBE clearing method allowed to reconstruct large specimens with a light sheet microscope. Since DBE dissolves glues used in the construction of objective lenses, a Nikon 20× air objective was used. As representative results, some images of the cerebellum of an L7-GFP mouse are presented. Both low-resolution images of the entire specimen and high-resolution details are shown (figure 7.2), in particular, it is possible to observe all the Purkinje neurons labeled with GFP.

Finally, a whole brain from an adult Thy1-GFP-M mouse, expressing GFP in a random sparse neuronal subset, was reconstructed. LSM high-resolution images allowed segmentation of neuronal processes. Figure 7.2 shows the reconstruction of a pyramidal neuron from the layer V of the cerebral cortex. It is possible to recognize the dendrite arbor, the cell body, and the axon.

7.2 TDE clearing method

After organic solvents evaluation, aqueous solutions were considered. As already discussed in the introduction each of the techniques present in literature has advantages and disadvantages that make it suitable for a particular analysis.

However, none of the listed processes allowed the use of multiple imaging modalities. To achieve this, a novel and versatile process to clear brain tissue was developed.

This new clearing method is based on 2-2' thiodioethanol (TDE) [18], a non-viscous, water-miscible compound. The refractive index (RI) of the clearing solution can be finely tuned between that of water (1.33) and that

Figure 7.2: **LSM imaging of DBE clarified specimen** (a) Panels show, from left to right, low and high resolution images of a L7-GFP mouse cerebellum. Scale bar = 1000 μm, 500 μm, 200μm (b) 3D reconstruction of a whole Thy1-GFP-M mouse brain. A pyramidal neuron from layer V of the cerebral cortex is segmented in green. Scale bar = 1000 μm, 200 μm, 50 μm.

of TDE (1.52) by mixing TDE with a water-based solution in varying ratios. 97% TDE was used for the first time as a mounting medium for cell cultures, then it was applied on invertebrate [19] and intestine [20]. In this work, TDE is used for brain tissue clearing.

7.2.1 TDE direct clearing for two-photon microscopy

The first target of the analysis was to demonstrate that TDE can be used for sample preparation for two-photon fluorescence microscopy by a direct clearing of the sample through the immersion of the specimen in the TDE solution.

Based on literature and previous studies, SeeDB, a water-based optical clearing protocol, was considered the preferred method for TDE clearing comparison. The clearing effects of TDE were characterized in terms of transparency and preservation of the sample.

(PFA)-fixed mouse brain sections of 1 mm thickness were incubated in solutions of increasing percentage of TDE in phosphate-buffered saline (PBS). TDE diffused rapidly and homogeneously through the tissue and after few hours sections became transparent. The transmittance of TDE-clarified samples was measured and compared with that of SeeDB (figure 7.3). Every solution showed a transmittance enhancement with longer wavelengths and an increasing percentage of TDE in the solution up to a percentage of 80% TDE/PBS. At this percentage the transmittance was comparable with that of SeeDB-cleared samples. TDE clearing dramatically decreased the incubation time needed for clearing slice (few hours), in comparison with SeeDB that required weeks. Another advantage of TDE was the low viscosity compared to that of SeeDB that makes it easy to handle.

Although, the transmittance was higher using a 80% TDE solution,

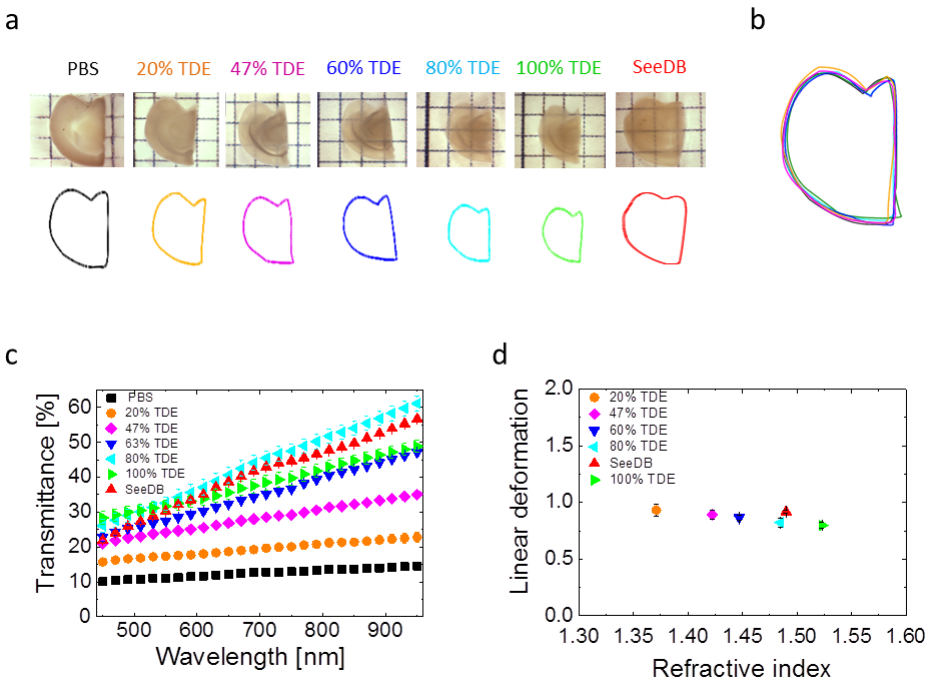

Figure 7.3: **Optical clearing with TDE** (a) Transmission images and edge tracing of 1 mm thick hemi-brain slices of Thy1-GFP-M mouse in PBS and after clearing with various solutions. (b) Superimposed image of the edges resized using the linear deformation parameter obtained in d, there is no anisotropic distortion. (c) Light transmittance curves of hemi-brain slices shown in a (mean ± s.e.m., n=4). (d) Normalized linear deformation during optical clearing (mean ± s.d., n=4). Image modified from Costantini et al. [71].

to perform two-photon fluorescence microscopy (TPFM) imaging, a 47% TDE/PBS solution was selected. It corresponds to the RI matched by the microscope objective used for imaging (Zeiss 20× Scale objective, with n=1.42). Using this concentration, it was demonstrated that TDE clearing did not cause significant linear deformation (10% shrinkage with 47% TDE/PBS solution) or anisotropic distortion of the tissue (figure 7.3).

Subsequently, to quantify the improvement of the imaging depth achievable in cleared samples, the contrast decay was measured as a function of depth in uncleared and cleared slices. The penetration depth with TPFM imaging in cleared tissue was almost four times higher than in samples uncleared (figure 7.4).

By measuring the fluorescence decay in cleared and uncleared tissue it was also demonstrated that incubation in TDE did not increase bleaching nor did it lead to quenching of protein fluorescence (figure 7.4). The fluorescence intensity remained constant over time, allowing long-term measurements for up to two months.

At last, transmission electron microscopy (TEM) imaging was performed to characterize the ultrastructure preservation of cleared samples (figure 7.5). TDE-treated samples were well preserved: nuclei, axons, dendrites, vesicles and organelles could be easily distinguished. Mitochondria appeared undamaged and ultrastructural features, such as synaptic vesicles and postsynaptic densities, were well preserved.

7.2.2 TDE-CLARITY clearing for light sheet microscopy

Since direct TDE incubation allowed to clear only thin sections, another protocol was developed for whole brain imaging. TDE was combined with the CLARITY method for light sheet microscopy analysis. Indeed, to obtain

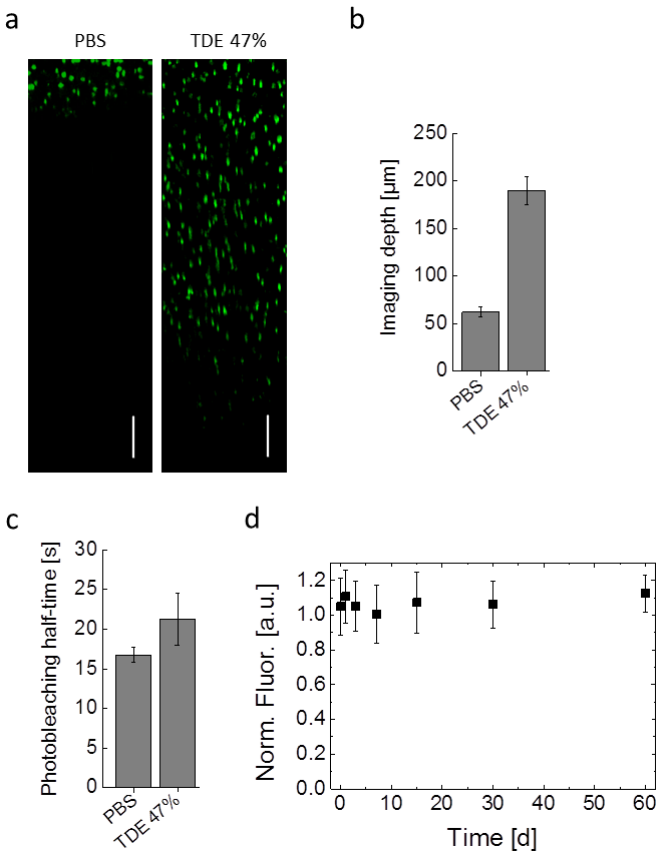

Figure 7.4: **Characterization of TDE clearing** (a) Two-photon fluorescence imaging of 2 mm FVB mouse brain slices stained with DAPI in PBS and in 47% TDE/PBS. Reconstruction along z-axis, depth 1 mm; scale bar = 100 μm. (b) Contrast decay as function of depth in uncleared and cleared samples (mean ± s.d., n=10). (c) Half-time fluorescence decay (mean ± s.d., n=4); clearing did not increase photobleaching compared to PBS. (d) Fluorescence intensity over time (mean ± s.d., n=10); no quenching effect was observed after incubation of the sample in 47% TDE/PBS for up to two months. Image modified from Costantini et al. [71].

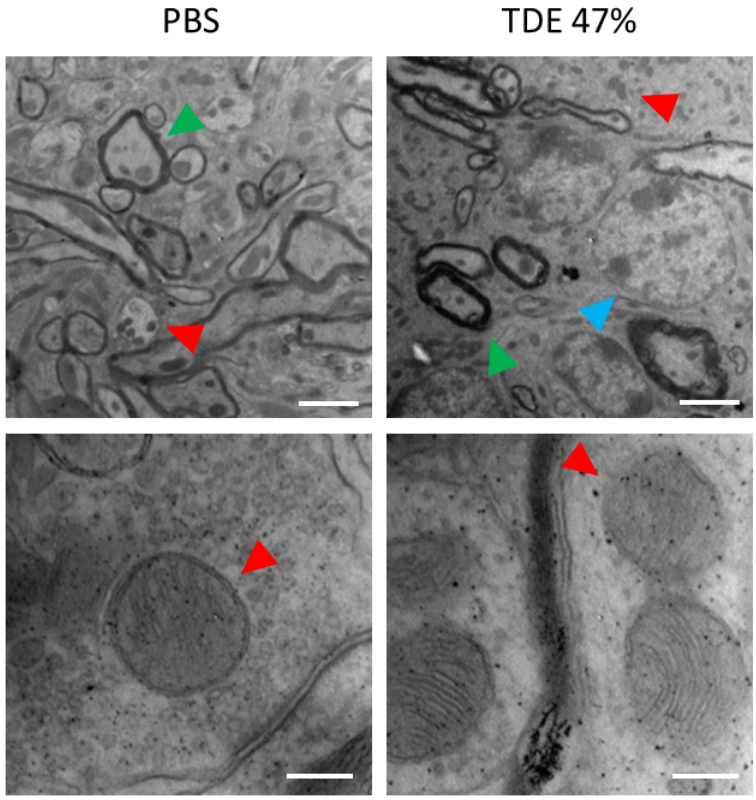

Figure 7.5: **Transmission electron microscopy** Images of Thy1-GFP-M mouse brain slices previously incubated in PBS and in 47% TDE/PBS for 4 days. Triangles indicate mitochondria (red), axons (green) and nuclei (blue). Scale bar = 2 μm (upper panels) and 200 nm (lower panels). Image taken from Costantini et al. [71].

an inexpensive tool to expand the applicability of light sheet microscopy, TDE was used as clearing agent instead of FocusClear^{TM} for the CLARITY protocol.

In order to match the correct refractive index (RI=1.45), a 63% TDE/PBS solution was selected. Entire CLARITY mouse brains were made uniformly transparent, and the transmittance was compared to that of FocusClear^{TM}. Moreover, the linear deformation and the anisotropic distortion of the tissue caused by the clearing were studied (figure 7.6).

During the analysis also the electrophoretic step of the CLARITY protocol was considered. During this step the tissue expands and then it comes back to the original size after clearing, producing a transient swelling. Tissue linear deformation caused by clearing with TDE and with FocusClear^{TM} was measured and compared. As result, it was noticed that TDE, similarly to FocusClear^{TM}, shrank the tissue back producing a final tissue expansion of 16% without introducing anisotropic distortion (figure 7.6).

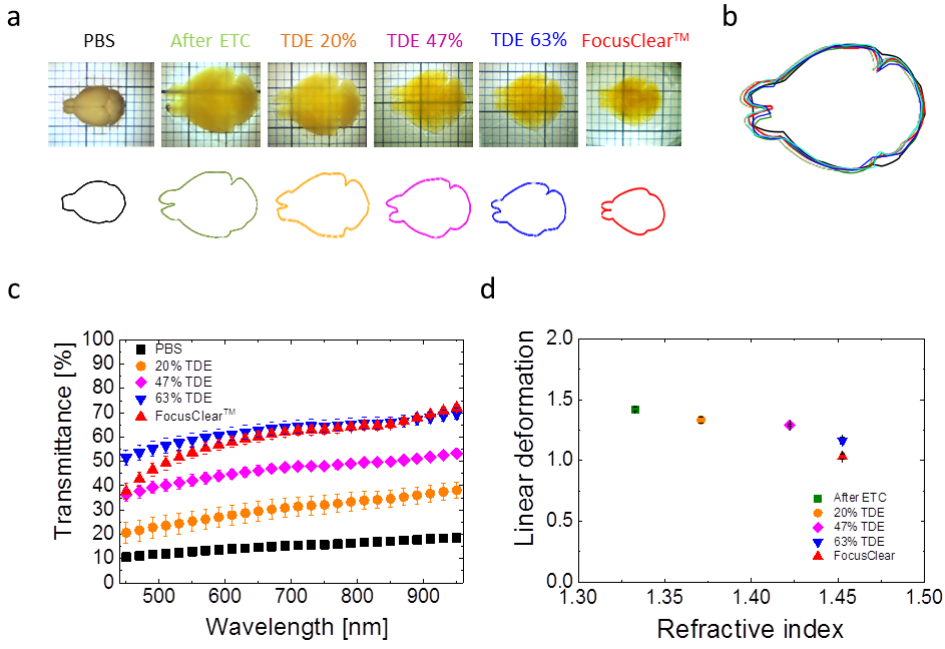

Figure 7.6: **Combination of the TDE clearing with the CLARITY protocol** (a) Transmission images and edge tracing of a Thy1-GFP-M mouse brain after CLARITY protocol: hydrogel-tissue hybridization and lipid removal with ETC, clearing with various solutions. (b) Superimposed image of the edges resized using the linear deformation parameter obtained in d, there is no anisotropic distortion. (c) The light transmittance of 2 mm CLARITY brain slices in different solutions (mean ± s.e.m, n=4). Transmittance increased with the RI and that of 63% TDE/PBS is comparable to that of FocusClear^{TM}. (d) Normalized linear deformation of CLARITY brains in different solutions (mean ± s.d, n=4). After initial expansion due to the ETC lipid removal, the tissue shrank back to its original size during the clearing step. Image modified from Costantini et al. [71].

Chapter 8

Mouse brain imaging with TDE clearing

TDE clearing, with or without the combination with the CLARITY protocol, was used to prepare specimens for serial two-photon tomography and light sheet microscopy. In particular, it was used to reduce the imaging time necessary to reconstruct a large tissue volume allowing fast analysis of mouse brain anatomy. This chapter will present the results obtained using the TDE clearing protocol for STP and LSM imaging.

8.1 Serial two-photon tomography

The direct TDE clearing was exploited to expand the imaging depth achievable with the serial two-photon tomography technique (STP). TDE clearing enhanced the penetration depth achievable with TPFM. Thus it allowed to reduce tissue slicing, decreased the acquisition time, minimized cut artifacts and enabled lossless whole sample imaging compared to the classic

STP used by Ragan et al. [14].

To demonstrate the capabilities of direct TDE clearing, an entire mouse hippocampus dissected from a fixed adult Thy1-GFP-M mouse brain was reconstructed. The hippocampus was imaged with TPFM using a Zeiss 20× Sca*l*e objective (figure 8.1).

Through this complete tomography, specific anatomical features of the hippocampus, such as dentate gyrus and Cornu Ammonis areas, were easily recognizable (figure 8.2). Moreover, the high-resolution stacks acquired in this tomography could reveal fine anatomical details of the sample such as spines and varicosities.

The high sensitivity of this approach enabled the complete tracing of single neurons through a large volume without interpolation as shown in figure 8.3.

8.2 Light sheet microscopy

After demonstrating the possibility of performing complete reconstruction of large volumes at high resolution, the aim of the work was addressed at getting an expanded view of morphological details over the whole mouse brain. The strength of the TDE clearing is the versatility that make it suitable for correlative approaches.

LSM, combined with suitable clearing techniques, has the potential of imaging big volumes of tissue in short time. Brains from different mouse lines were thus processed with CLARITY and cleared with TDE in order to imaged them with LSM.

At first an adult PV-cre-tdTomato mouse brain, in which parvabuminergic neurons are labeled with the tdTomato fluorescent protein, was reconstructed with sub-cellular resolution. As shown in figure 8.4 the main

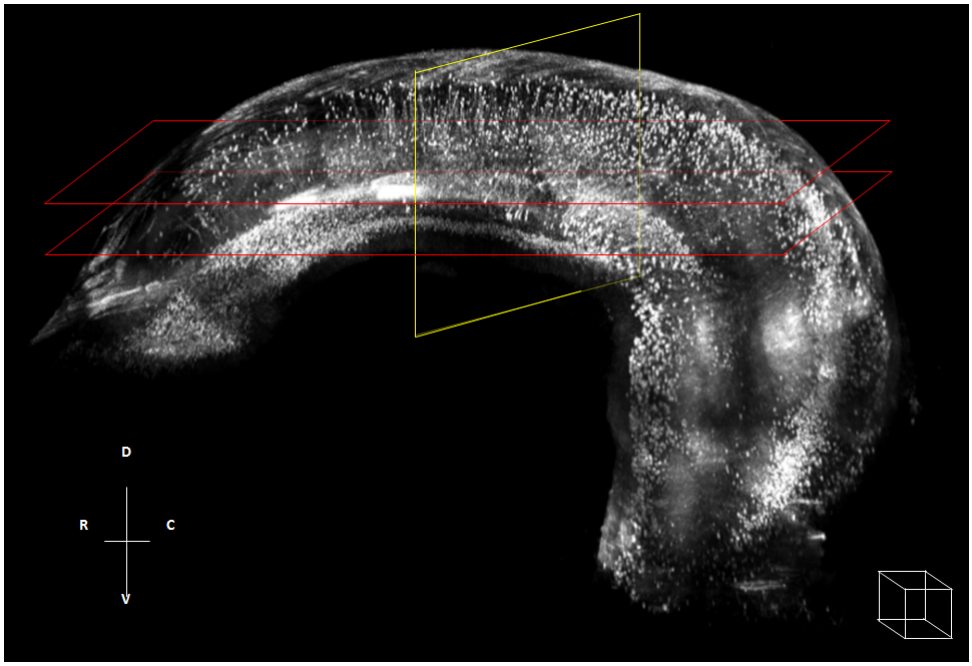

Figure 8.1: **Hippocampus tomography** Reconstruction of entire Thy1-GFP-M mouse hippocampus fixed with PFA and cleared with 47% TDE/4PBS (Zeiss 20× Sca*l*e objective, two-photon excitation). 3D rendering of six layers of 1 mm thickness each sampled every 4 μm. Serial sectioning at 800 μm depth. The scale of the figure can be inferred from the white cube in the bottom right corner which has 300 μm side. Image taken from Costantini et al. [71].

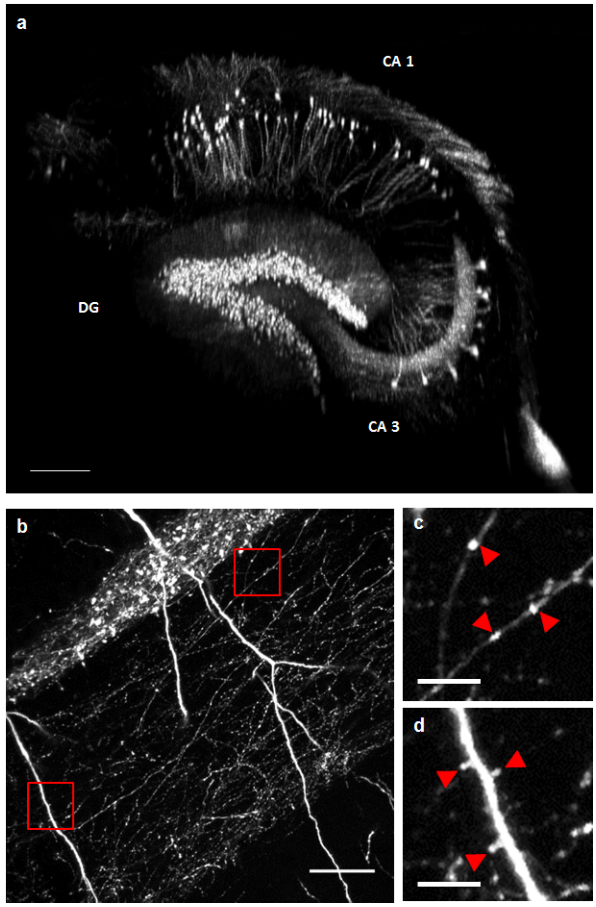

Figure 8.2: **Hippocampus high resolution images** (a) Coronal section corresponding to the yellow box in 8.1. It is possible to recognize the dentate gyrus (DG) and the Cornu Ammonis areas (CA1 and CA3); scale bar = 300 μm. (b) Single image at full resolution of one stack showing some dendritic and axonal fibers; scale bar = 50 μm. (c) and (d) Magnified inserts corresponding to red boxes in c. Red triangles highlight axon varicosities and dendritic spines; scale bar = 10 μm. Image taken from Costantini et al. [71].

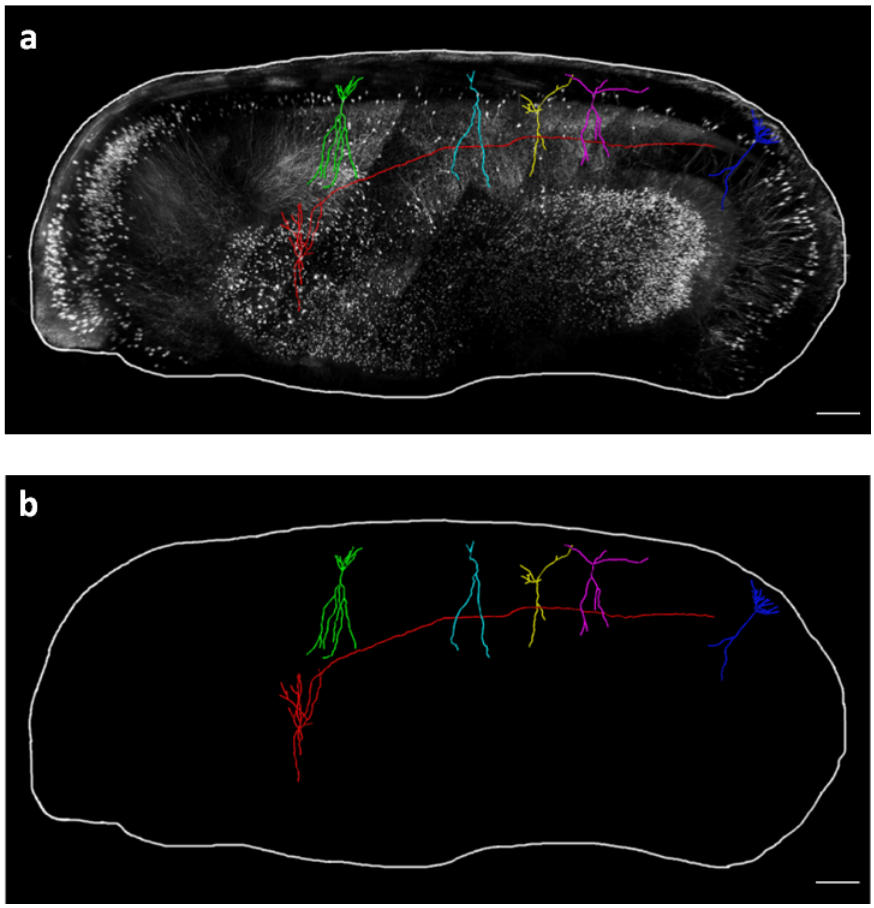

Figure 8.3: **Neuron tracing** Three-dimensional tracing of single neurons through different stacks and layers of the hippocampus shown in 8.1. Image a shows a maximum intensity projection of a volume of 400 μm, while in b there are only the neuron tracks. Scale bar = 300 μm. Image taken from Costantini et al. [71].

anatomical features can be easily dissected and the distribution of cells bodies and axonal bundles can be visualized over the whole brain.

The preservation of the sample was also maintained in a GAD2-cre-tdTomato mouse brain, in which GABAergic interneurons are labeled, showing finer details of the neuronal connections (figure 8.5). To further test the compatibility of this clearing method with organic dyes, a mouse brain labeled with the nuclear cell marker propidium iodide was imaged (figure 8.5). The fluorescence of this molecule was retained over the whole brain. In future, this could be used to provide valuable data for automatic cell body counting algorithms [72].

Finally, brain vasculature (previously labeled with FITC-albumin) was imaged. This approach revealed even the smaller capillaries, allowing access to large volumetric reconstructions of the mouse vasculature (figure 8.5).

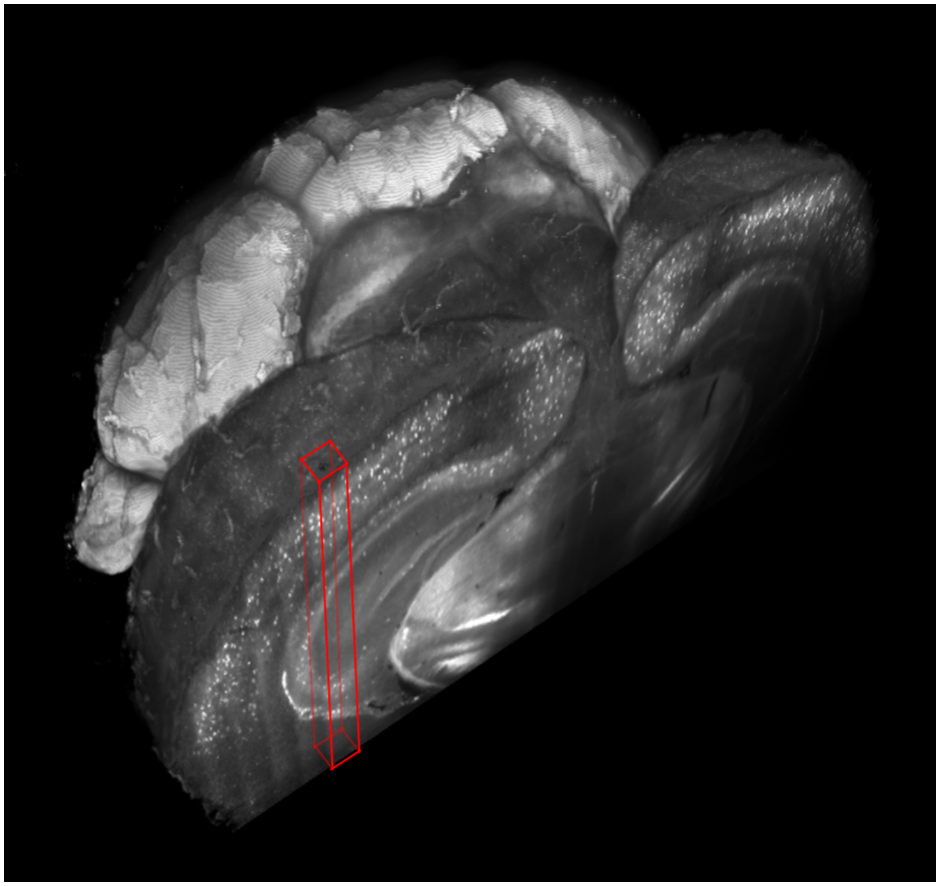

Figure 8.4: **Whole mouse brain tomography** Imaging of whole PV-tdTomato transgenic mouse brains treated with CLARITY and cleared with 63% TDE/PBS imaged with LSM (Olympus, 25× objective). Image taken from [71].

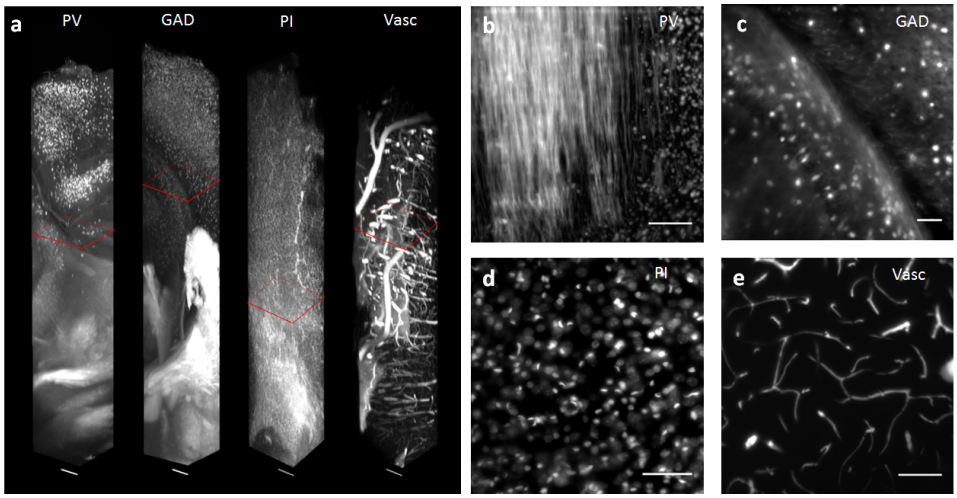

Figure 8.5: **LSM mouse brains imaging** (a) 3D rendering of stacks from a PV-tdTomato mouse brain, a GAD-tdTomato mouse brain, a PI stained mouse brain, and aFITC-albumin labeled mouse brain, scale bar = 400 μm. (b,c,d,e) High-resolution inserts of stack corresponding to red boxes in a. Scale bar = 100 μm. Image taken from [71].

Chapter 9

Human brain imaging

After demonstrating the general applicability of the TDE method on animal models, its translational potential was investigated on human samples. Human brain studies present various challenges. This chapter will describe some of them. In particular, sample preparation, large tissue labeling, sample clearing, and imaging will be described.

9.1 Tissue immunostaining

Human brain analysis with fluorescence microscopy requires an *ex vivo* labeling. A technique that allows specific labeling is immunohistochemistry (IHC). Usually, it is performed on thin slices (10 μm thick) because the membrane lipid double-layer prevents antibody penetration into tissues. CLARITY overcomes this limitation by removing lipids, allowing IHC on large samples. To permit thick brain tissue labeling with immunohistochemistry, the compatibility of TDE clearing with the use of antibodies was investigated.

At first, the compatibility of TDE clearing with immunohistochemistry was tested on mouse brain tissue. A slice of a PFA-fixed Thy1-GFP-M mouse brain was treated with the passive CLARITY (PC) method [21]. The sample preparation used in this protocol allowed to obtain the CLARITY hydrogel without the direct perfusion of acrylamide. Proteins are embedded in the gel while lipids are removed with passive clearing.

The sample was labeled with an Alexa Fluor 594 conjugated anti-GFP antibody and then cleared with the 47% TDE/PBS solution before TPFM imaging. GFP and Alexa Fluor signals colocalized showing that the labeling was well performed. The characteristic features of GFP-expressing neurons (for example dendritic spines) were easily recognizable in the TPFM images (figure 9.1), suggesting that the 47% TDE/PBS solution did not affect the protein-antibody interaction.

After proving that TDE is a valid clearing medium for mouse IHC stained tissue, the protocol was applied on human brain samples.

A large specimen surgically removed from a patient with drug resistant epilepsy due to hemimegalencephaly (HME) was studied. The sample exhibiting the severe form of cortical dysplasia suits the purpose of testing the method's sensitivity in highlighting different elements of an abnormal cytoarchitectonic organization.

In particular, a 2-mm thick block of the cortex, stored in formalin, was treated with the PC technique, stained with different antibodies and cleared with TDE solution. The tissue was successfully labeled with antibodies against parvalbumin (PV) and glial fibrillary acidic protein (GFAP) as well as a double labeling with the combination of them (figure 9.2).

The CLARITY method allows multi-round analysis on mouse brain. In this work it was successfully adapted to human brain tissue analysis. Indeed, a 2-mm thick block of the cortex was labeled with anti-PV antibody, cleared

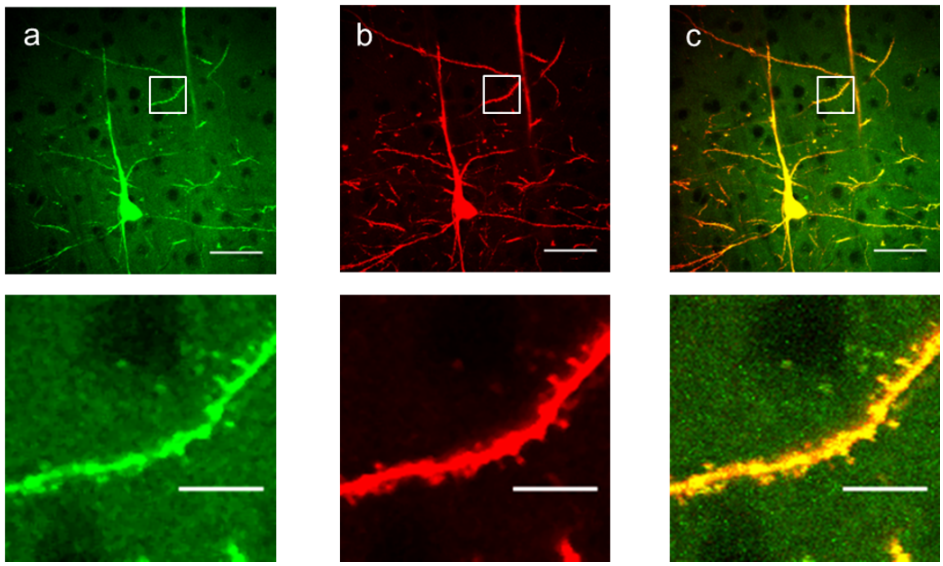

Figure 9.1: **Mouse brain immunostaining** TDE-CLARITY clearing is compatible with IHC. (a) GFP fluorescence (green); (b) Alexa Fluor 594 anti-GFP antibody (red); (c) overlay. Scale bar = 50 μm (upper panels) and 10 μm (lower panels). Image taken from Costantini et al. [71].

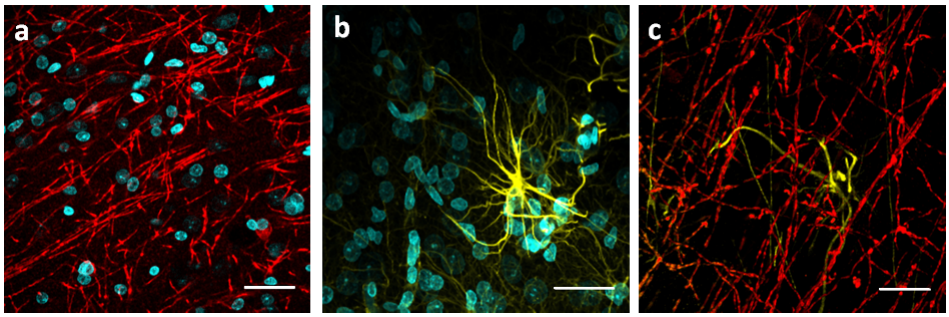

Figure 9.2: **Multiple immunostaining** Human brain labeling with different antibodies. (a) Parvalbumin (PV) staining in red and nuclei (DAPI) in cyan; scale bar = 100 μm. (b) Glial fibrillary acidic protein (GFAP) staining in yellow and nuclei (DAPI) in cyan; scale bar = 100 μm. (c) GFAP staining in yellow and PV in red; scale bar = 100 μm. Image taken from [71].

with TDE and imaged with TPFM, and then PV antibodies were removed and the tissue was stained again with anti-GFAP antibodies and imaged with TPFM (figure 9.3).

9.2 Three-dimensional reconstruction of the cortex of a patient with hemimegalencephaly

The development of the cerebral cortex is a complexly organized process. Disruption of any of the steps that contribute to this process (neuronal proliferation, migration or layer organization), can result in a wide range of developmental disorders.

Many of these disorders are recognized as malformations of cortical development (MCD). MCD encompasses a wide spectrum of focal and diffuse disorders with various underlying genetic etiologies and clinical manifesta-

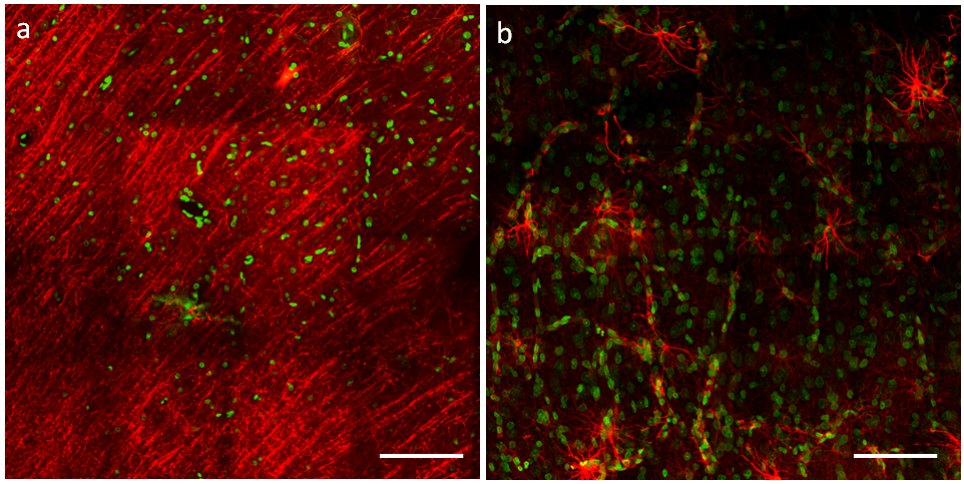

Figure 9.3: **Multi-round immunostaining** (a) Parvalbumin (PV) staining in red and nuclei (DAPI) in green; scale bar = 100 μm. (b) Glial fibrillary acidic protein (GFAP) staining in red and nuclei (DAPI) in green; scale bar = 100 μm.

tions [73, 74, 75]. Hemimegalencephaly (HME), first described by Sims in 1835 [76], also known as unilateral megalencephaly, is a malformation of the cortex, that occurs during the early development and is characterized by the enlargement of one cerebral hemisphere (figure 9.4) [77, 78, 79].

An HME cerebral cortex presents several histopathological abnormalities: dyslamination, dysmorphic immature neurons and balloon cells, indicating primary defects in neuroglial differentiation, migration and cellular growth [73]. HME is considered to be a primary disorder of proliferation wherein the neurons that are unable to form synaptic connections are not eliminated but accumulated [73]. The affected hemisphere may also have focal or diffuse neuronal and glial cell migration defects. The exact pathogenesis of such a complex malformation is still unknown.

Individuals with HME typically present epilepsy, psychomotor disability, contralateral hemiparesis, and hemianopsia. Treatments may lessen or alleviate seizures and improve the quality of life for HME patients. In most cases, the first line of treatment is AEDs (Anti-Epileptic Drugs), though many children experience significant benefit from hemispherectomy. Hemispherectomy is the most effective treatment to control seizures, and it also seems to provide good results on the psychomotor development when performed early [80].

After proving the compatibility of TDE clearing with PC and IHC, the protocol was used to characterized the specimen removed from a patient with drug resistant epilepsy due to hemimegalencephaly (HME). In particular alterations of the cerebral cortex were imaged and three-dimensional information on neuronal organization were obtained.

To validate the process, dysplastic tissue images obtained with the new protocol were compared with that of routine anatomopathological characterization. This evaluation allowed a direct comparison between con-

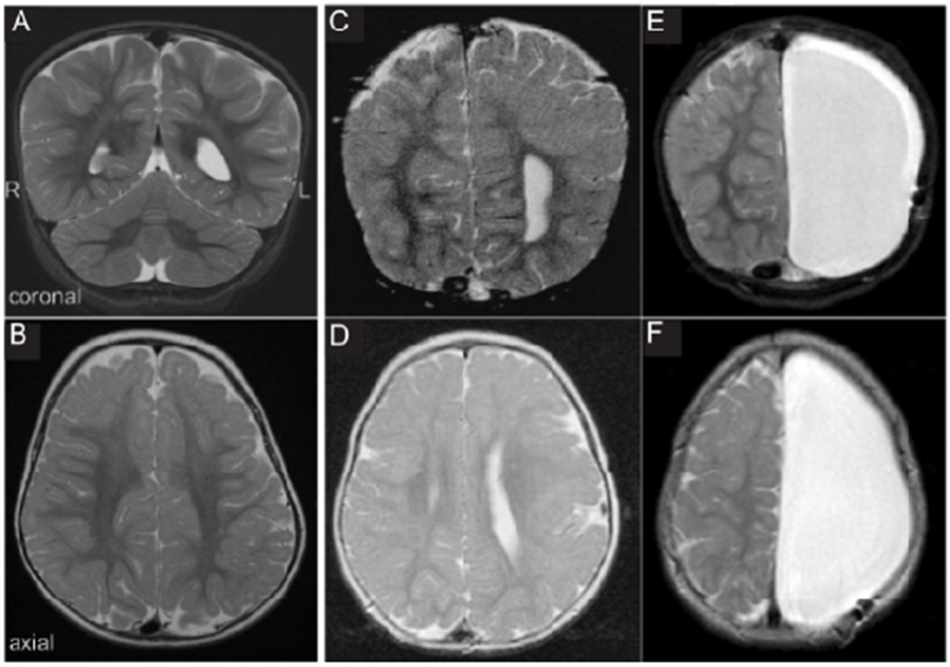

Figure 9.4: **MRIs of a patient with hemimegalencephaly (HME)** (a,b) Coronal and axial MRI images showing a normal brain. (c,d) MRI images from the brain of a patient with HME, before the surgical removal of the left-sided abnormal hemisphere. (e,f) Images of the brain after left hemispherectomy. Cerebrospinal fluid fills the space where the abnormal hemisphere had been. From [79].

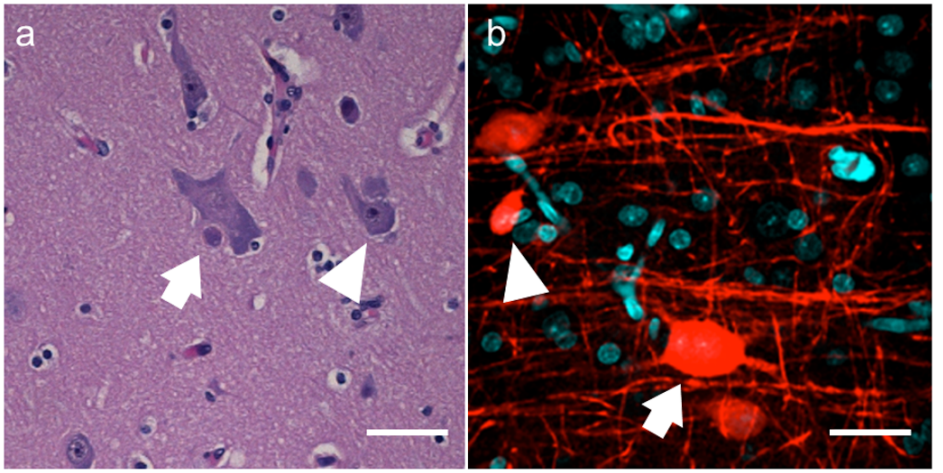

Figure 9.5: **Human brain histology** (a) Hematoxylin/eosin staining of paraffin embedded tissue (b) Two-photon imaging of the sample treated with the passive-CLARITY protocol, cleared with TDE and immunostained with anti-parvalbumin (in red) and nuclei marker (DAPI, in cyan). White arrows indicate giant dysmorphic neurons, white arrowheads indicate wild-type neurons. Scale bar = 50 μm. Image taken from [71].

ventional hematoxylin/eosin staining and the immunostaining obtained on TDE-CLARITY cleared sample.

Giant dysmorphic neurons were identified using both staining techniques, remarking that the features observed in the cleared tissue were directly comparable to those obtained by conventional staining techniques (figure 9.5).

To obtain three-dimensional information of the dysplastic tissue a cube of 1 mm^3 was prepared and imaged with TPFM. The staining was performed with an antibody against parvalbumin in combination with DAPI (figure 9.6). To analyze the homogeneity of the labeling through the tissue during

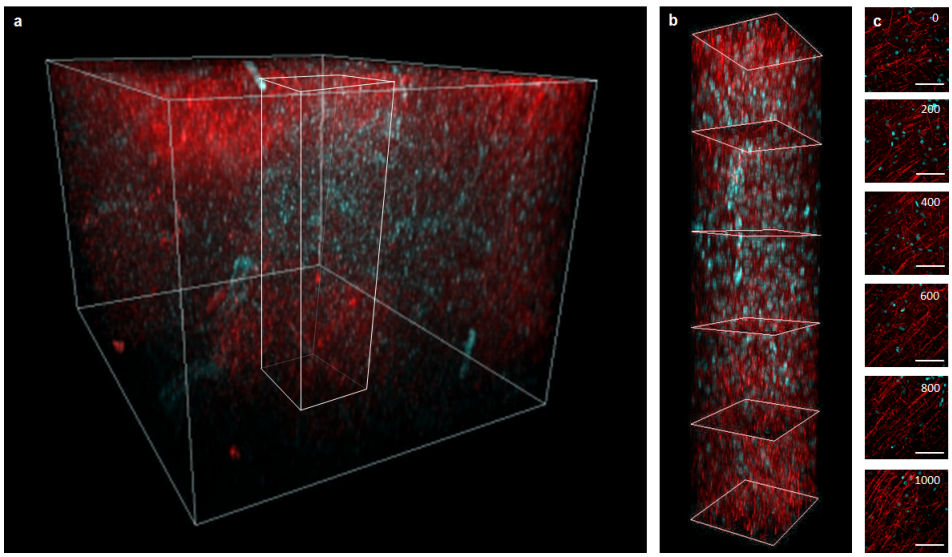

Figure 9.6: **Human brain 3D reconstruction** 2 mm thick block of formalin-fixed tissue removed from the dysplastic hemisphere of a patient with hemimegalencephaly, treated with PC CLARITY protocol, immunostained and cleared with 47% TDE/PBS (Zeiss 20× Scale objective, two-photon excitation).(a,b) 3D rendering of a $1 \times 1 \times 1$ mm^3 and $0.25 \times 0.25 \times 1$ mm^3 section of brain tissue labeled for PV (red) and DAPI (cyan). (c) Horizontal view of sections of b at different depths; scale bar = 100 μm. Image taken from [71].

imaging the same contrast was maintained through out the whole depth. The result showed that optimization of the PC staining protocol with the introduction of the TDE clearing allowed augmenting the penetration depth of the antibody by 100% compared to the data of Chung et al [21].

No alterations in signal intensity were observed over the entire depth. Moreover, single axons could be easily recognized in the densely labeled sample. Tracing of neurons could be performed across the entire volume (figure 9.7). Isolated neuronal processes could be clearly distinguished, demonstrating that projections can now be studied by tracing neurites over a mm-sized volume.

Finally, the structural alteration of the whole cortex of the HME patient was observed. The PV-stained tissue was imaged, and a mosaic was performed starting from the gray matter and ending at the white matter. Figure 9.8 shows the organization of neuronal fibers: the gray matter presents a high concentration of strands, the white matter, instead, is constituted by well organized fibers. Indeed, it is possible to observe by eyes their precise orientation. It is also possible to identify some dimorphic cells body, mainly located 3 mm below the gray matter.

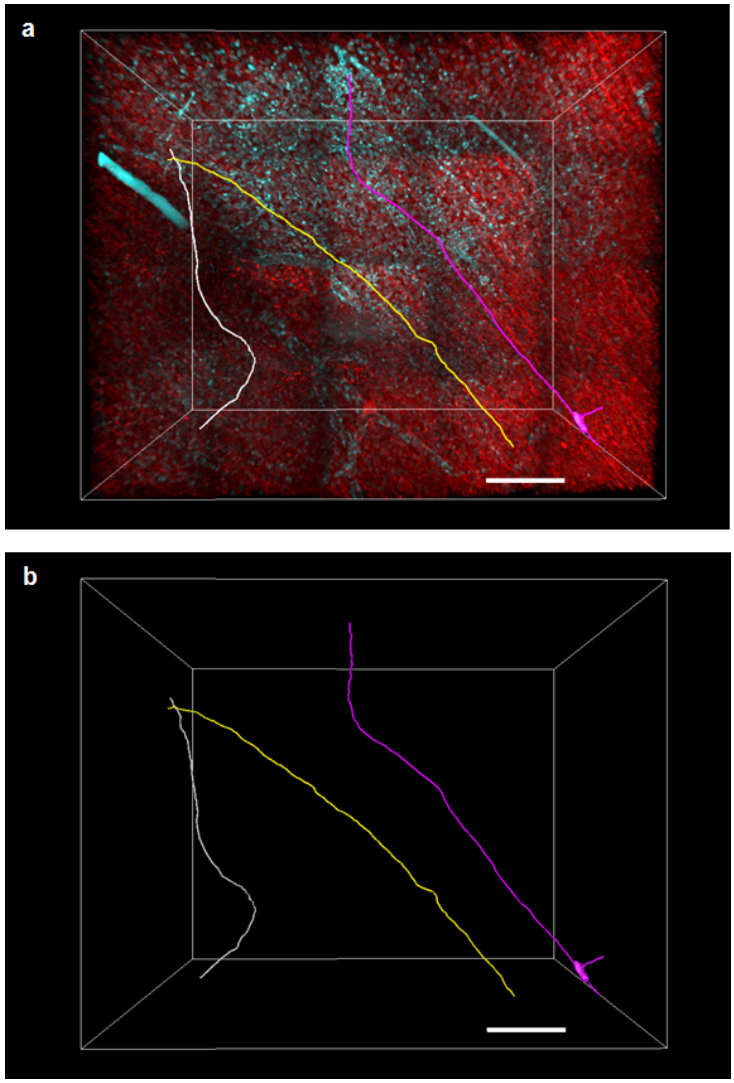

Figure 9.7: **Neuronal tracing** Three-dimensional tracing of parvalbumin fibers through the volume shown in 9.6. Scale bar = 200 μm. Image taken from [71].

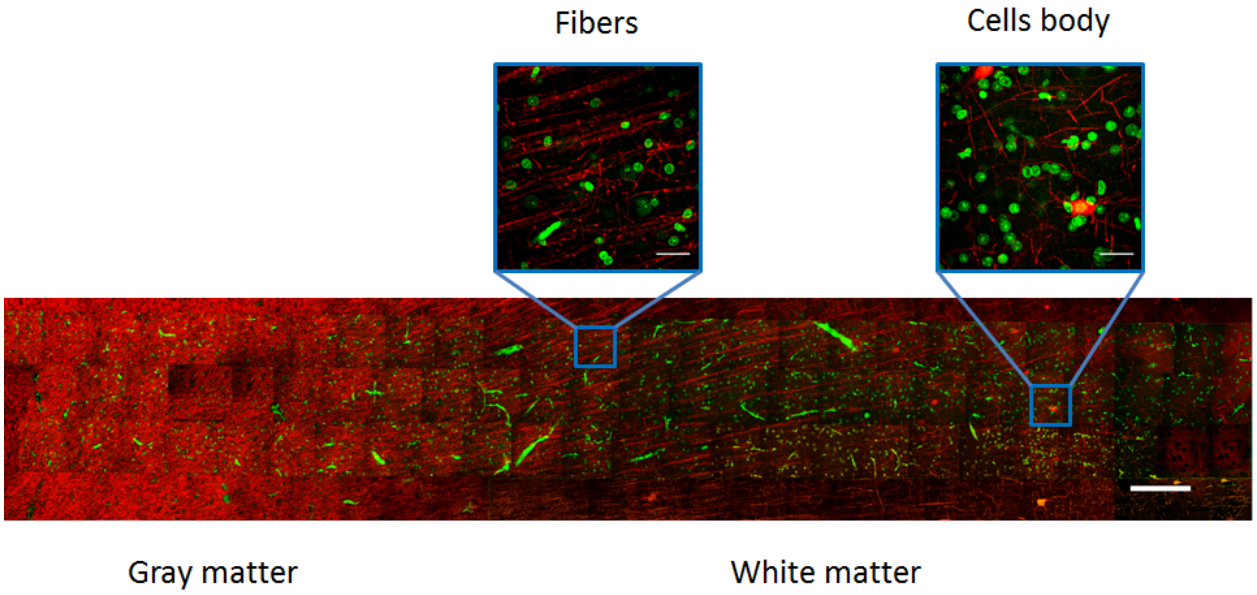

Figure 9.8: **Human brain cortex** Mosaic of MIPs (depth = 10 μm) of the cortex removed from the dysplastic hemisphere of a patient with hemimegalencephaly immunostained for PV in red and DAPI in green (Zeiss 20× Scale objective, two-photon excitation). From left to right it is possible to distinguish the gray matter and the white matter. The white matter is characterized by the presence of well oriented fibers. It is also possible to see some cell bodies. Scale bar= 300 μm, blue insets = 50 μm.

Part IV

Conclusions

Chapter 10

Discussion

Commonly, optical dissection of brain architecture is addressed with different microscopy techniques coupled with various sample preparation methods. In this respect, several clearing protocols have been developed to reduce light scattering during imaging. Table 10.1 summarizes the major techniques developed in the last years based on both organic and aqueous solutions. However, each of them has distinctive characteristics which makes it suitable for a specific optical technique while limiting its use for complementary ones. These characteristics confine the research to a specific field, preventing the possibility of using multi-modal approaches. Although these techniques can study specific questions, they are not enough to address the connectomics challenge. Indeed, to do that it is necessary to combine different methods and integrate the data obtained with various techniques. The purpose of this thesis is exactly obtaining a tool that facilitates correlative approaches. In this chapter the results obtained in this respect are discussed with the help of the current literature.

The evaluation of organic solvents clearing confirms what was suggested

Method	Clearing Composition	Refractive Index	Corrected Objective Available	Linear Deformation	Protein Fluorescence quencing	Sample Appearance	High Viscosity	Cost*	Clearing Time	IHC	Clearing Capability	References
Et + BABB	Ethanol Benzyl alcohol Benzyl Benzoate	1.56	No	Shrinkage	Yes	Stiff	No	$	2 days	No	Good	[16]
3DISCO	Thetrahydrofiuran Dibenzyl ether	1.56	No	Shrinkage	Yes In same days	Stiff	No	$	2 days	No	Good	[48] [49]
iDISCO	Thetrahydrofiuran Dibenzyl ether	1.56	No	Shrinkage	Yes In some days	Stiff	No	$$	2 days	Yes	Good	[50]
Glycerol	Glycerol solution	1.44	Yes	No	No	/	Yes	$	2 days	No	Moderate	/
Scale	Urea Glycerol Triton X-100	1.38	Yes	Expansion	No	Fragile	No	$	Months	No	Moderate	[51]
Clear^T	Formamide	1.45	Yes	Swelling	No	/	No	$	1 day	No	Moderate	[52]
SeeDB	Fructose α thioglycerol	1.49	Yes	No	No	/	Yes	$	2 weeks	No	Moderate	[53]
CUBIC	Urea Aminoalcohols	1.47	Yes	Transient swelling	No	/	No	$	2 weeks	Yes	Good	[54] [55]
RIMs (PACT)	Histodenz	1.38-1.48	Yes	Slight expansion	No	/	No	$$$	2 weeks	Yes	Good	[54] [59]
FRUIT	Fructose Urea	1.48	Yes	Minimal expansion	No	/	No	$	5 days	No	Good	[54] [59]
CLARITY	FocusClear^{TM}	1.45	Yes	Transient swelling	No	Spongy	No	$$$	10 days	Yes	Good	[21]
TDE	2,2' Thiodioethanol	Tunable	Yes	No	No	/	No	$	2 hours	No	Moderate	[71]
CARITY + TDE	2,2' Thiodioethanol	Tunable	Yes	Transient swelling	No	Spongy	No	$$	10 days	Yes	Good	[71]

Table 10.1: **Comparison of different clearing methods** This table gives an overview of the available techniques reported in the literature and their limitations and advantages. *Cost per sample is considered for both labeling and clearing. It is indicated as inexpensive ($) if less than $50, medium ($$) if between $50 and $500, and expensive ($$$) for over $500 per sample.

in the work of Becker et al. [48]. Tetrahydrofuran with dibenzyl ether is indeed the best combination of dehydration and clearing solvents used to prepare samples. This approach allows for imaging samples with good resolution, moreover, it is fast and easy to perform, and it can be applied to immunolabelled samples (as shown in the iDISCO techniques [50]).

However, it presents some limitation: first of all, after a few days the protein fluorescence is quenched, making long measurements unfeasible in transgenic animals with normal fluorescent protein expression levels. Secondly, the process is irreversible: every sample can be used only for one type of study, it is not possible to analyze the sample with different techniques. Eventually, DBE dissolves glues used in the construction of objective lenses, preventing the use of immersion objectives that avoid aberrations introduced by the air/solvent interface. The absence of commercial corrected objectives for DBE [81] limits the quality of the acquired images affecting the results.

To overcome the limitations found using the organic solvent clearing, this thesis faced the development of a simple, quick and inexpensive clearing method for multi-modal brain imaging. The method was based on a refractive index matching agent called 2,2'-thiodiethanol (TDE) [18].

The first application consisted in the direct incubation of samples in TDE solutions for two-photon fluorescence microscopy. The TDE clearing was compared with another method present in literature, the SeeDB [53] technique. It was considered a better clearing techniques compared to others (table 10.1), because SeeDB does not introduce tissue deformation and preserves fluorescence of the sample.

The clearing characterization, performed on PFA-fixed tissue, was based on several criteria. Resulting transparency in terms of light transmittance, protein fluorescence quenching and bleaching, linear deformation and

anisotropic distortion of the tissue. Tests showed that the transparency attainable was comparable with that of SeeDB. It depended on the RI of the solution and, therefore, on the increasing concentration of TDE in the solutions. In particular, the imaging depth achievable after the clearing procedure was increased by a factor of four in PFA-fixed samples compared with uncleared tissues.

During the process, clearing did not substantially change the final volume of the specimen, nor did it lead to linear deformation or anisotropic distortion. Moreover protein fluorescence of the sample remained constant over time during long-term incubations, even up to months, indicating that the clearing protocol does not lead to quenching. Also, it did not lead to fluorescence bleaching, therefore, it is suitable for the study of protein endogenous fluorescence in transgenic animals conversely to the organic solvent techniques [16] [48]. Nevertheless TDE diffuses quickly inside the brain tissue, allowing a fast and easy clearing procedure compared with other techniques such as, for example, Sca*l*e [51] or SeeDB [53] (see table 10.1).

Finally, a very important characteristic of TDE is the low-viscosity of the solutions. It allows easy sample sectioning, making TDE clearing suitable for the complete reconstruction of large brain areas using serial two-photon tomography (STP). On the contrary, the SeeDB method is incompatible with STP due to its high viscosity. This limits the acquisition of 3D volumes to the imaging depth reached by the microscope.

The advantages given by the TDE direct clearing were used to study an entire PFA-fixed Thy1-GFP-M mouse hippocampus. The combination of acquired stacks using an automatic 3D-stitching tool allowed to trace single neuronal processes with high accuracy throughout entire volume. Thanks to the reconstruction of the tomography, every individual part of the hippocampus was imaged at high resolution, giving the possibility to resolve

spines and varicosities across the whole area.

TDE direct clearing, however, is not suitable for the imaging of entire organs without cutting. Hence to overcome this limit and to obtain an optimum transparency in the whole mouse brain, TDE was coupled with the CLARITY technique [21] to allow imaging with light sheet microscopy.

It was demonstrated that TDE is a valid alternative to FocusClear^{TM} as refractive index matching solution. It considerably lowers the cost of every experiment and makes affordable large-volume, high-throughput imaging with LSM possible.

Moreover, the unknown composition of FocusClear^{TM} impaired any effort of the scientific community to further improve its clearing efficiency. Instead, TDE permits the integration of other compounds that can potentially improve the optical transparency of the selected specimen. Moreover the refractive index variation achievable by different TDE/PBS percentages allows an ad hoc optimization of the clearing capability of the method for different tissue types.

To demonstrate the applicability of the TDE-CLARITY protocol, mouse brains labeled with different dyes were imaged with LSM. Both neurons and vessels were studied, as well as cell nuclei and fibers. The different applications underline how TDE can be used for various analysis, from the three dimensional organization of a subpopulation of neurons (e.g. the parvalbuminergic or the GABAergic system) to the localization of every cell of the brain, but also the arrangement of the vascular system.

Finally, the compatibility of TDE clearing with immunostaining on brain tissue from different species was studied, namely on mouse brain and human brain samples. The protocol was implemented for formalin-fixed samples and combined with the passive CLARITY. A 1 mm^3 cube of tissue from a hemimegalencephaly patient was homogenously stained with differ-

ent antibodies and imaged with TPFM. Dysplastic neurons, characteristic of the disease [73], were recognized; moreover, neuronal fibers were followed throughout the whole volume.

The capability of performing immunochemistry in a large volume of human brain tissue with micrometric resolution and high sensitivity is a crucial step in the direction of human brain connectomics. Moreover, it represents an innovative translational tool to characterize macroscopic and microscopic circuit alterations and to identify cells having aberrant morphology, that are a common finding in brains of individuals with refractory epilepsy, intellectual disability, and autism.

In conclusion, compared with other techniques, the TDE protocol covers a wide range of applications. The most intriguing characteristic of this method lies in its versatility; the possibility to choose the most suitable tool for different experiments permits a powerful investigation of neuronal networks in the brain. As a matter of fact, TDE can facilitate correlative approaches and help to overcome the inherent limitations of a single imaging technique, enabling multi-modal approaches for brain anatomy studies [82, 83]. It can, definitely, contribute to enhancing the understanding of anatomic structure and connectomics of the brain.

For the future, the usefulness of TDE may not be limited only to brain neuroanatomy investigations but, as shown by other clearing methods, could also span different areas of research such as entomology [16] [84], embryology [48] [15] and even medicine with 3D anatomical studies of biopsies from different organs and tissues [21].

Chapter 11

Future prospective

The work of this thesis approaches the connectomics challenge by expanding the possibility of performing multi-modal analysis on mouse and human brains. However, to obtain a complete view of the brain a lot of work remains to be done. This chapter describes some improvements that could be accomplished in the near future that will facilitate anatomical analysis.

As first analysis, the limitations of the TDE technique in the field of human brain imaging needs to be explored. In particular, to expand the human study, future work should regard the maximum sample thickness achievable with the immunostaining technique. The best compromise between contrast (which is limited by the penetration depth of antibodies) and sample throughput should be studied. After that, using the optimized TDE technique the neurons organization will be mapped in healthy and pathological human brains. Through the development of a software for automatic cell localization and tracing the differences between samples will be studied and quantitative data will be obtained. That will give the possibility to exploit new diagnostic methods based on three-dimensional analysis.

Thanks to great advances in optics, different microscopes are now commercially available, leading to the necessity of having useful techniques for sample preparation. In particular, clearing procedures, as the one presented in this work, are crucial in obtaining high tissue transparency while preserving sample fluorescence. Up to now a lot of different approaches have been explored, however, for the future, the main goal to pursue will be the standardization of protocols, rather than the development of new ones. Indeed, commercial kits could remove systematic errors obtaining more reliable results [85].

In parallel, other potential developments concern the correction of light scattering within the microscope. In fact, instead of operating only on sample preparation, it can be possible to correct aberration using techniques such as adaptive optics. The combination of adaptive optics with sample clearing will increase acquisition speed, will extend imaging depth penetration and will improve the spatial resolution of future optical microscopes [86, 87].

Another big challenge of neuroanatomy reconstruction regards sample labeling. Transgenic fluorescent animal models are widely used to study brain structures. However, the use of genetically encoded fluorescent indicators is limited to a few animal models and requires complex genetic engineering procedures. To expand fluorescence microscopy to different types of samples, such as a pathological model or human brain, it is necessary to develop new techniques. Antibodies and nucleic acids conjugated with fluorescent indicators may be used to access all different kinds of specimen. They should be optimized to better access epitopes deep inside samples in a short period of time. A promising recent development in this field is the engineering of nucleic acid aptamers and single-domain antibodies [88]. Additionally, new methods can be developed to substitute the passive dif-

fusion of molecules inside tissue, for example, active transport can facilitate penetration making the labeling fast and uniform [89].

A different important aspect that will require a lot of effort regards the management of the large data sets obtained with image acquisitions. 3D reconstructions of whole specimens from raw data as well as analysis and comparison between different massive volumetric data sets take a considerable amount of processing time and computational memory. To achieve a global organization of the information, it will be necessary to develop novel technologies as for massive data collection, data sharing, and multi-modal integration so to achieve statistically robust conclusions [90].

Finally, to obtain a complete view of the brain, efforts need to be focused on correlation with functional analysis. Structural reconstruction can't give all the information necessary to understand how the brain works. It is extremely important to integrate it with functional maps of brain circuitry that can now be achieved at the mesoscale level with approaches such as MRI [91, 92, 93] which can investigate the connections between different brain areas. Moreover, electrophysiological analysis of single neuronal activity can be done with electrodes or through the combination of optogenetic technology [94, 95] with optical recording mediated by voltage sensitive dyes or calcium indicators.

Such efforts are highly informative, indeed, to comprehend how neural circuits process information and generate behavior, it will be necessary to connect all the different studies. When a high level of spatial and temporal resolution analysis will be collected in one single map, the connectomics challenge could eventually be solved.

Bibliography

[1] R. C. Craddock, R. L. Tungaraza, and M. P. Milham. Connectomics and new approaches for analyzing human brain functional connectivity. *Gigascience*, 4:13, 2015. 3

[2] O. Sporns, G. Tononi, and R. Kotter. The human connectome: A structural description of the human brain. *PLoS Comput Biol*, 1(4): e42, 2005. 3

[3] https://www.humanbrainproject.eu/. 4

[4] http://www.braininitiative.nih.gov/. 4

[5] K. L. Briggman and D. D. Bock. Volume electron microscopy for neuronal circuit reconstruction. *Curr Opin Neurobiol*, 22(1):154–61, 2012. 4

[6] S. Mori and J. Zhang. Principles of diffusion tensor imaging and its applications to basic neuroscience research. *Neuron*, 51(5):527–39, 2006. 4

[7] L. Silvestri, L. Sacconi, and F. S. Pavone. The connectomics challenge. *Funct Neurol*, 28(3):167–73, 2013. 5

[8] Mertz J. *Introduction to optical microscopy.* Roberts and company publishers, 2010. 5, 20, 24

[9] J. Livet, T. A. Weissman, H. Kang, R. W. Draft, J. Lu, R. A. Bennis, J. R. Sanes, and J. W. Lichtman. Transgenic strategies for combinatorial expression of fluorescent proteins in the nervous system. *Nature*, 450(7166):56–62, 2007. 5

[10] J. E. Berlier, A. Rothe, G. Buller, J. Bradford, D. R. Gray, B. J. Filanoski, W. G. Telford, S. Yue, J. Liu, C. Y. Cheung, W. Chang, J. D. Hirsch, J. M. Beechem, R. P. Haugland, and R. P. Haugland. Quantitative comparison of long-wavelength alexa fluor dyes to cy dyes: fluorescence of the dyes and their bioconjugates. *J Histochem Cytochem*, 51(12):1699–712, 2003. 5

[11] R. Loesel, S. Weigel, and P. Braunig. A simple fluorescent double staining method for distinguishing neuronal from non-neuronal cells in the insect central nervous system. *J Neurosci Methods*, 155(2):202–6, 2006. 5

[12] A. Li, H. Gong, B. Zhang, Q. Wang, C. Yan, J. Wu, Q. Liu, S. Zeng, and Q. Luo. Micro-optical sectioning tomography to obtain a high-resolution atlas of the mouse brain. *Science*, 330(6009):1404–8, 2010. 5, 30

[13] H. Gong, S. Zeng, C. Yan, X. Lv, Z. Yang, T. Xu, Z. Feng, W. Ding, X. Qi, A. Li, J. Wu, and Q. Luo. Continuously tracing brain-wide long-distance axonal projections in mice at a one-micron voxel resolution. *Neuroimage*, 74:87–98, 2013. 5, 30

[14] T. Ragan, L. R. Kadiri, K. U. Venkataraju, K. Bahlmann, J. Sutin, J. Taranda, I. Arganda-Carreras, Y. Kim, H. S. Seung, and P. Osten. Serial two-photon tomography for automated ex vivo mouse brain imaging. *Nat Methods*, 9(3):255–8, 2012. 5, 6, 30, 31, 33, 92

[15] J. Huisken, J. Swoger, F. Del Bene, J. Wittbrodt, and E. H. Stelzer. Optical sectioning deep inside live embryos by selective plane illumination microscopy. *Science*, 305(5686):1007–9, 2004. 5, 31, 118

[16] H. U. Dodt, U. Leischner, A. Schierloh, N. Jahrling, C. P. Mauch, K. Deininger, J. M. Deussing, M. Eder, W. Zieglgansberger, and K. Becker. Ultramicroscopy: three-dimensional visualization of neuronal networks in the whole mouse brain. *Nat Methods*, 4(4):331–6, 2007. 5, 31, 38, 40, 55, 79, 114, 116, 118

[17] P. J. Keller and H. U. Dodt. Light sheet microscopy of living or cleared specimens. *Curr Opin Neurobiol*, 22(1):138–43, 2012. 5

[18] T. Staudt, M. C. Lang, R. Medda, J. Engelhardt, and S. W. Hell. 2,2'-thiodiethanol: a new water soluble mounting medium for high resolution optical microscopy. *Microsc Res Tech*, 70(1):1–9, 2007. 6, 81, 115

[19] P. L. Appleton, A. J. Quyn, S. Swift, and I. Nathke. Preparation of wholemount mouse intestine for high-resolution three-dimensional imaging using two-photon microscopy. *J Microsc*, 234(2):196–204, 2009. 6, 83

[20] P. T. Gonzalez-Bellido and T. J. Wardill. Labeling and confocal imaging of neurons in thick invertebrate tissue samples. *Cold Spring Harb Protoc*, 2012(9):969–83, 2012. 6, 83

[21] K. Chung, J. Wallace, S. Y. Kim, S. Kalyanasundaram, A. S. Andalman, T. J. Davidson, J. J. Mirzabekov, K. A. Zalocusky, J. Mattis, A. K. Denisin, S. Pak, H. Bernstein, C. Ramakrishnan, L. Grosenick, V. Gradinaru, and K. Deisseroth. Structural and molecular interrogation of intact biological systems. *Nature*, 497(7449):332–7, 2013. 6, 45, 46, 47, 48, 62, 67, 100, 108, 114, 117, 118

[22] Jessell T.M. Kandel E.R., Schwartz J.H. *Principles of neural science*. Number 4th ed in Principles of neural science 4th ed. McGraw-Hill, 2000. 9, 10, 12, 14, 16, 18

[23] D. Purves. *Neuroscience*. Number 4th ed in . Sinauer Associates, 2004. 9, 12, 14

[24] M. W. Barnett and P. M. Larkman. The action potential. *Pract Neurol*, 7(3):192–7, 2007. 11

[25] T. Sasaki, N. Matsuki, and Y. Ikegaya. Action-potential modulation during axonal conduction. *Science*, 331(6017):599–601, 2011. 11

[26] Segal M. Pickel V. M. *The Synapse: Structure and Function*. Elselvier, 2014. 12

[27] Nieto-Sampedro M. Castellano Lopez B. *Glial Cell Function*. Elselvier, 2004. 12

[28] http://www.webmd.com/. 15

[29] L. Heimer. *The Human Brain and Spinal Cord: Functional Neuroanatomy and Dissection Guide*. Number 2nd ed. in The Human Brain and Spinal Cord: Functional Neuroanatomy and Dissection Guide. Springer, 1994. 16, 17, 18

[30] N. Spruston. Pyramidal neurons: dendritic structure and synaptic integration. *Nat Rev Neurosci*, 9(3):206–21, 2008. 16

[31] L.D. Fricker. *Neuropeptides and Other Bioactive Peptides: From Discovery to Function*. Morgan and Claypool Publishers, 2012. 16

[32] J. W. Lichtman and J. A. Conchello. Fluorescence microscopy. *Nat Methods*, 2(12):910–9, 2005. 21, 22

[33] J.R. Lakowicz. *Principles of fluorescence spectroscopy*. Number v. 1 in Principles of Fluorescence Spectroscopy. Springer, 2006. 21

[34] http://www.olympusmicro.com/. 24

[35] E. Hecht. *Optics*. Number 2nd ed. in . Addison Wesley, 1987. 25, 38

[36] Silvestri L. Confocal ultramicroscopy:micron-scale neuroanatomy of the entire mouse brain. *PhD Thesis*, 20. 27

[37] J.B. Pawley. *Handbook of biological confocal microscopy. Language of science.* Number v. 1 in Handbook of biological confocal microscopy. Language of science. Springer, 2006. 26

[38] W. R. Zipfel, R. M. Williams, and W. W. Webb. Nonlinear magic: multiphoton microscopy in the biosciences. *Nat Biotechnol*, 21(11): 1369–77, 2003. 28, 29

[39] F. Helmchen and W. Denk. Deep tissue two-photon microscopy. *Nat Methods*, 2(12):932–40, 2005. 28, 29, 30

[40] K. Svoboda and R. Yasuda. Principles of two-photon excitation microscopy and its applications to neuroscience. *Neuron*, 50(6):823–39, 2006. 30

[41] P. Osten and T. W. Margrie. Mapping brain circuitry with a light microscope. *Nat Methods*, 10(6):515–23, 2013. 32

[42] J. Huisken and D. Y. Stainier. Selective plane illumination microscopy techniques in developmental biology. *Development*, 136(12):1963–75, 2009. 31, 35

[43] U. Leischner, W. Zieglgansberger, and H. U. Dodt. Resolution of ultramicroscopy and field of view analysis. *PLoS One*, 4(6):e5785, 2009. 31

[44] D. S. Richardson and J. W. Lichtman. Clarifying tissue clearing. *Cell*, 162(2):246–57, 2015. 38

[45] Huffman D. R. Bohren C.F. *Absorption and Scattering of Light by Small Particles*. Wiley, 1983. 38

[46] Kao F. Torok P. *Optical imaging and microscopy*. Number 2nd ed. in . Springer, 2007. 38

[47] W. Spalteholz. *Uber das Durchsichtigmachen von menschlichen und tierischen Praparaten*. Uber das Durchsichtigmachen von menschlichen und tierischen Praparaten. S. Hierzel, 1914. 38, 40

[48] K. Becker, N. Jahrling, S. Saghafi, R. Weiler, and H. U. Dodt. Chemical clearing and dehydration of gfp expressing mouse brains. *PLoS One*, 7 (3):e33916, 2012. 40, 42, 55, 58, 79, 114, 115, 116, 118

[49] A. Erturk, K. Becker, N. Jahrling, C. P. Mauch, C. D. Hojer, J. G. Egen, F. Hellal, F. Bradke, M. Sheng, and H. U. Dodt. Three-dimensional imaging of solvent-cleared organs using 3disco. *Nat Protoc*, 7(11):1983–95, 2012. 40, 41, 79, 114

[50] N. Renier, Z. Wu, D. J. Simon, J. Yang, P. Ariel, and M. Tessier-Lavigne. idisco: a simple, rapid method to immunolabel large tissue samples for volume imaging. *Cell*, 159(4):896–910, 2014. 40, 114, 115

[51] H. Hama, H. Kurokawa, H. Kawano, R. Ando, T. Shimogori, H. Noda, K. Fukami, A. Sakaue-Sawano, and A. Miyawaki. Scale: a chemical approach for fluorescence imaging and reconstruction of transparent mouse brain. *Nat Neurosci*, 14(11):1481–8, 2011. 42, 114, 116

[52] T. Kuwajima, A. A. Sitko, P. Bhansali, C. Jurgens, W. Guido, and C. Mason. Cleart: a detergent- and solvent-free clearing method for neuronal and non-neuronal tissue. *Development*, 140(6):1364–8, 2013. 42, 114

[53] M. T. Ke, S. Fujimoto, and T. Imai. Seedb: a simple and morphology-preserving optical clearing agent for neuronal circuit reconstruction. *Nat Neurosci*, 16(8):1154–61, 2013. 42, 43, 72, 114, 115, 116

[54] E. A. Susaki, K. Tainaka, D. Perrin, F. Kishino, T. Tawara, T. M. Watanabe, C. Yokoyama, H. Onoe, M. Eguchi, S. Yamaguchi, T. Abe, H. Kiyonari, Y. Shimizu, A. Miyawaki, H. Yokota, and H. R. Ueda. Whole-brain imaging with single-cell resolution using chemical cocktails and computational analysis. *Cell*, 157(3):726–39, 2014. 44, 114

[55] K. Tainaka, S. I. Kubota, T. Q. Suyama, E. A. Susaki, D. Perrin, M. Ukai-Tadenuma, H. Ukai, and H. R. Ueda. Whole-body imaging with single-cell resolution by tissue decolorization. *Cell*, 159(4):911–24, 2014. 44, 114

[56] B. Hou, D. Zhang, S. Zhao, M. Wei, Z. Yang, S. Wang, J. Wang, X. Zhang, B. Liu, L. Fan, Y. Li, Z. Qiu, C. Zhang, and T. Jiang.

Scalable and dii-compatible optical clearance of the mammalian brain. *Front Neuroanat*, 9:19, 2015. 44

[57] H. Hama, H. Hioki, K. Namiki, T. Hoshida, H. Kurokawa, F. Ishidate, T. Kaneko, T. Akagi, T. Saito, T. Saido, and A. Miyawaki. Scales: an optical clearing palette for biological imaging. *Nat Neurosci*, 18(10): 1518–29, 2015. 44

[58] R. Tomer, L. Ye, B. Hsueh, and K. Deisseroth. Advanced clarity for rapid and high-resolution imaging of intact tissues. *Nat Protoc*, 9(7): 1682–97, 2014. 45

[59] B. Yang, J. B. Treweek, R. P. Kulkarni, B. E. Deverman, C. K. Chen, E. Lubeck, S. Shah, L. Cai, and V. Gradinaru. Single-cell phenotyping within transparent intact tissue through whole-body clearing. *Cell*, 158 (4):945–58, 2014. 49, 114

[60] G. Feng, R. H. Mellor, M. Bernstein, C. Keller-Peck, Q. T. Nguyen, M. Wallace, J. M. Nerbonne, J. W. Lichtman, and J. R. Sanes. Imaging neuronal subsets in transgenic mice expressing multiple spectral variants of gfp. *Neuron*, 28(1):41–51, 2000. 53

[61] H. Taniguchi, M. He, P. Wu, S. Kim, R. Paik, K. Sugino, D. Kvitsiani, Y. Fu, J. Lu, Y. Lin, G. Miyoshi, Y. Shima, G. Fishell, S. B. Nelson, and Z. J. Huang. A resource of cre driver lines for genetic targeting of gabaergic neurons in cerebral cortex. *Neuron*, 71(6):995–1013, 2011. 53

[62] L. Madisen, T. A. Zwingman, S. M. Sunkin, S. W. Oh, H. A. Zariwala, H. Gu, L. L. Ng, R. D. Palmiter, M. J. Hawrylycz, A. R. Jones, E. S. Lein, and H. Zeng. A robust and high-throughput cre reporting and

characterization system for the whole mouse brain. *Nat Neurosci*, 13 (1):133–40, 2010. 53

[63] F. Biamonte, G. Assenza, R. Marino, M. D'Amelio, R. Panteri, D. Caruso, S. Scurati, J. G. Yague, L. M. Garcia-Segura, R. Cesa, P. Strata, R. C. Melcangi, and F. Keller. Interactions between neuroactive steroids and reelin haploinsufficiency in purkinje cell survival. *Neurobiol Dis*, 36(1):103–15, 2009. 53

[64] L. Silvestri, A. Bria, I. Costantini, L. Sacconi, H. Peng, G. Iannello, and F. S. Pavone. Micron-scale resolution optical tomography of entire mouse brains with confocal light sheet microscopy. *J Vis Exp*, (80), 2013. 56

[65] L. Silvestri, A. Bria, L. Sacconi, G. Iannello, and F. S. Pavone. Confocal light sheet microscopy: micron-scale neuroanatomy of the entire mouse brain. *Opt Express*, 20(18):20582–98, 2012. 57

[66] A. L. Mascaro, I. Costantini, E. Margoni, G. Iannello, A. Bria, L. Sacconi, and F. S. Pavone. Label-free near-infrared reflectance microscopy as a complimentary tool for two-photon fluorescence brain imaging. *Biomed Opt Express*, 6(11):4483–4492, 2015. 59, 60

[67] M. C. Mullenbroich, L. Silvestri, L. Onofri, I. Costantini, M. V. Hoff, L. Sacconi, G. Iannello, and F. S. Pavone. Comprehensive optical and data management infrastructure for high-throughput light-sheet microscopy of whole mouse brains. *Neurophotonics*, 2(4):041404, 2015. 65, 66

[68] A. Bria and G. Iannello. Terastitcher - a tool for fast automatic 3d-stitching of teravoxel-sized microscopy images. *BMC Bioinformatics*, 13:316, 2012. 68

[69] P. J. Keller, A. D. Schmidt, A. Santella, K. Khairy, Z. Bao, J. Wittbrodt, and E. H. Stelzer. Fast, high-contrast imaging of animal development with scanned light sheet-based structured-illumination microscopy. *Nat Methods*, 7(8):637–42, 2010. 74

[70] G. W. Knott, A. Holtmaat, J. T. Trachtenberg, K. Svoboda, and E. Welker. A protocol for preparing gfp-labeled neurons previously imaged in vivo and in slice preparations for light and electron microscopic analysis. *Nat Protoc*, 4(8):1145–56, 2009. 74

[71] I. Costantini, J. P. Ghobril, A. P. Di Giovanna, A. L. Allegra Mascaro, L. Silvestri, M. C. Mullenbroich, L. Onofri, V. Conti, F. Vanzi, L. Sacconi, R. Guerrini, H. Markram, G. Iannello, and F. S. Pavone. A versatile clearing agent for multi-modal brain imaging. *Sci Rep*, 5: 9808, 2015. 84, 86, 87, 89, 93, 94, 95, 97, 98, 101, 102, 106, 107, 109, 114

[72] P. Frasconi, L. Silvestri, P. Soda, R. Cortini, F. S. Pavone, and G. Iannello. Large-scale automated identification of mouse brain cells in confocal light sheet microscopy images. *Bioinformatics*, 30(17):i587–93, 2014. 96

[73] I. Blumcke, M. Thom, E. Aronica, D. D. Armstrong, H. V. Vinters, A. Palmini, T. S. Jacques, G. Avanzini, A. J. Barkovich, G. Battaglia, A. Becker, C. Cepeda, F. Cendes, N. Colombo, P. Crino, J. H. Cross, O. Delalande, F. Dubeau, J. Duncan, R. Guerrini, P. Kahane, G. Math-

ern, I. Najm, C. Ozkara, C. Raybaud, A. Represa, S. N. Roper, N. Salamon, A. Schulze-Bonhage, L. Tassi, A. Vezzani, and R. Spreafico. The clinicopathologic spectrum of focal cortical dysplasias: a consensus classification proposed by an ad hoc task force of the ilae diagnostic methods commission. *Epilepsia*, 52(1):158–74, 2011. 104, 118

[74] R. Guerrini and R. Carrozzo. Epilepsy and genetic malformations of the cerebral cortex. *Am J Med Genet*, 106(2):160–73, 2001. 104

[75] R. Guerrini and W. B. Dobyns. Malformations of cortical development: clinical features and genetic causes. *Lancet Neurol*, 13(7):710–26, 2014. 104

[76] J. Sims. On hypertrophy and atrophy of the brain. *Med Chir Trans*, 19:315–80, 1835. 104

[77] S. T. Baek, E. M. Gibbs, J. G. Gleeson, and G. W. Mathern. Hemimegalencephaly, a paradigm for somatic postzygotic neurodevelopmental disorders. *Curr Opin Neurol*, 26(2):122–7, 2013. 104

[78] J. H. Lee, M. Huynh, J. L. Silhavy, S. Kim, T. Dixon-Salazar, A. Heiberg, E. Scott, V. Bafna, K. J. Hill, A. Collazo, V. Funari, C. Russ, S. B. Gabriel, G. W. Mathern, and J. G. Gleeson. De novo somatic mutations in components of the pi3k-akt3-mtor pathway cause hemimegalencephaly. *Nat Genet*, 44(8):941–5, 2012. 104

[79] A. Poduri, G. D. Evrony, X. Cai, P. C. Elhosary, R. Beroukhim, M. K. Lehtinen, L. B. Hills, E. L. Heinzen, A. Hill, R. S. Hill, B. J. Barry, B. F. Bourgeois, J. J. Riviello, A. J. Barkovich, P. M. Black, K. L. Ligon, and C. A. Walsh. Somatic activation of akt3 causes hemispheric

developmental brain malformations. *Neuron*, 74(1):41–8, 2012. 104, 105

[80] M. J. De Rosa, D. L. Secor, M. Barsom, R. S. Fisher, and H. V. Vinters. Neuropathologic findings in surgically treated hemimegalencephaly: immunohistochemical, morphometric, and ultrastructural study. *Acta Neuropathol*, 84(3):250–60, 1992. 104

[81] K. Becker, C. M. Hahn, S. Saghafi, N. Jahrling, M. Wanis, and H. U. Dodt. Reduction of photo bleaching and long term archiving of chemically cleared gfp-expressing mouse brains. *PLoS One*, 9(12):e114149, 2014. 115

[82] L. Silvestri, A. L. Allegra Mascaro, I. Costantini, L. Sacconi, and F. S. Pavone. Correlative two-photon and light sheet microscopy. *Methods*, 66(2):268–72, 2014. 118

[83] A. L. Allegra Mascaro, P. Cesare, L. Sacconi, G. Grasselli, G. Mandolesi, B. Maco, G. W. Knott, L. Huang, V. De Paola, P. Strata, and F. S. Pavone. In vivo single branch axotomy induces gap-43-dependent sprouting and synaptic remodeling in cerebellar cortex. *Proc Natl Acad Sci U S A*, 110(26):10824–9, 2013. 118

[84] N. Jahrling, K. Becker, C. Schonbauer, F. Schnorrer, and H. U. Dodt. Three-dimensional reconstruction and segmentation of intact drosophila by ultramicroscopy. *Front Syst Neurosci*, 4:1, 2010. 118

[85] http://www.logosbio.com/. 120

[86] K. Wang, D. E. Milkie, A. Saxena, P. Engerer, T. Misgeld, M. E. Bronner, J. Mumm, and E. Betzig. Rapid adaptive optical recovery of

optimal resolution over large volumes. *Nat Methods*, 11(6):625–8, 2014. 120

[87] M. J. Booth. Adaptive optics in microscopy. *Philos Trans A Math Phys Eng Sci*, 365(1861):2829–43, 2007. 120

[88] D. H. Bunka and P. G. Stockley. Aptamers come of age - at last. *Nat Rev Microbiol*, 4(8):588–96, 2006. 120

[89] S. Y. Kim, E. Murray, J.H. Cho, N. Bakh, K. Ohn, and K. Chung. Rapid and quantitative phenotyping of intact biological systems. *Society for Neuroscience*, Washington(7449):332–7, 2014. 121

[90] F. Engert. The big data problem: turning maps into knowledge. *Neuron*, 83(6):1246–8, 2014. 121

[91] W. Hollingworth, C. J. Todd, M. I. Bell, Q. Arafat, S. Girling, K. R. Karia, and A. K. Dixon. The diagnostic and therapeutic impact of mri: an observational multi-centre study. *Clin Radiol*, 55(11):825–31, 2000. 121

[92] P. K. Woodard, D. A. Bluemke, P. N. Cascade, J. P. Finn, A. E. Stillman, C. B. Higgins, R. D. White, E. K. Yucel, and Radiology American College of. Acr practice guideline for the performance and interpretation of cardiac magnetic resonance imaging (mri). *J Am Coll Radiol*, 3(9):665–76, 2006. 121

[93] L. Leksell, D. Leksell, and J. Schwebel. Stereotaxis and nuclear magnetic resonance. *J Neurol Neurosurg Psychiatry*, 48(1):14–8, 1985. Leksell. 121

[94] K. Deisseroth. Optogenetics. *Nat Methods*, 8(1):26–9, 2011. 121

[95] E. Pastrana. Sensors and probes: All-in-one optogenetics. *Nat Methods*, 10(1):16, 2013. 121